https://doi.org/10.5194/egusphere-2025-6186
Preprint. Discussion started: 2 February 2026

Composite Sharpening by Vortex Symmetrization and Normalization of Tropical Cyclones

Andrina Caratsch, Sylvaine Ferrachat, and Ulrike Lohmann

Institute for Atmospheric and Climate Science, ETH Zurich, Switzerland

Correspondence: Andrina Caratsch (andrina.caratsch@env.ethz.ch) and Ulrike Lohmann (ulrike.lohmann@env.ethz.ch)

Abstract. Cyclone composites are a powerful tool for investigating the mean characteristics of tropical and extratropical cyclones, offering insights into the mechanisms driving storm development. Traditional composite methods align cyclone centers to capture persistent patterns but they tend to smooth out small-scale features.

We introduce a novel compositing framework, the SYmmetrized-Normalized Cyclone (SyNC) compositing, designed to address the structural variety of tropical cyclones (TCs). This method symmetrizes storms to axisymmetric vortices and normalizes them according to their eyewall location and the size of the TC. By accurately detecting the eyewalls and the horizontal extents of TCs, the SyNC method enables detailed storm structural analysis. The method is applied to simulated TCs with the weather and climate model ICON, which show strong agreement with the observed wind–pressure relationships. ICON reveals the ability to simulate even most intense storms, while overestimating the frequency of major hurricanes. A large structural variability and asymmetries are found across all simulated storm intensities, agreeing with observations and emphasizing the importance of SyNC composites.

The vortex alignment of the SyNC framework successfully sharpens composite fields, preserving small-scale features such as super-gradient winds, subsidence within the eye, eyewall updrafts, and localized diabatic heating and cooling related to cloud microphysics. It also reduces within-group variance, thereby increasing statistical power and enabling the detection of differences between TC groups that would be missed using traditional center-based compositing. Limitations of the SyNC composites include reduced applicability during early storm stages, when tangential winds have not yet formed a Rankine-like vortex, and potential data extrapolation during normalization in small storms. Nonetheless, the method proves robust for weakly organized storms and is particularly beneficial for analyzing circulation-related and cloud microphysics-related fields. Overall, the SyNC compositing method provides a cyclone-relative framework that improves the accuracy of TC composite analysis, thereby facilitating the investigation and understanding of storm development.

https://doi.org/10.5194/egusphere-2025-6186
Preprint. Discussion started: 2 February 2026

1 Introduction

Cyclone composites are widely used to analyze mean characteristics of groups of tropical and extratropical cyclones to improve the understanding of their development and structure (Vessey et al., 2022; Sinclair et al., 2020; Klotz and Jiang, 2017; Bengtsson et al., 2007, 2009; Binder et al., 2016; Dacre et al., 2012; Wei et al., 2025; Sun et al., 2019; Ming et al., 2015; Trier et al., 2023). Cyclone composites are usually calculated by taking the average of a cyclone group at a particular stage of their life cycles after aligning the cyclone centers (Binder et al., 2016; Dacre et al., 2012; Sinclair et al., 2020; Bengtsson et al., 2007; Hanley et al., 2001; Trier et al., 2023). Some composite methods include the projection of each cyclone to the intersection of the Equator and the prime meridional to make cyclones located at different latitudes more comparable (Vessey et al., 2022). Extratropical cyclone fields are often rotated towards their propagation direction to better preserve their key structures, for example conveyor belts (Sinclair et al., 2020; Vessey et al., 2022). For similar reasons, tropical cyclones (TCs) are sometimes rotated according to their storm motion or to the environmental vertical wind shear (VWS) (Klotz and Jiang, 2017; Rios-Berrios and Torn, 2017; Uhlhorn et al., 2014; Zhang et al., 2013; Carstens et al., 2024). Storm motion increases the tangential wind field asymmetry by contributing to the wind speed where the storm's tangential wind vectors and translation vectors align, typically on the right side of the storm track (Uhlhorn et al., 2014). VWS influences the storm structure by increasing the tangential and radial wind asymmetry (Klotz and Jiang, 2017; Carstens et al., 2024), which is further associated with asymmetric surface fluxes and asymmetric convection (Zhang et al., 2013; Carstens et al., 2024). However, depending on the research focus, TC composites can also not be rotated, when for example studying the interactions with upper-tropospheric troughs (Hanley et al., 2001). Generally, cyclone composites capture persistent patterns well but tend to smooth out small-scale features (Bengtsson et al., 2007, 2009; Binder et al., 2016; Dacre et al., 2012; Vessey et al., 2022). The smoothing can be caused by misalignment of the storm's structures, when the compositing TC group contains various storm sizes and vortex axis-asymmetries, while only aligning the TC centers. Indeed, observed TCs reveal various vortex sizes and are rarely geometrically axisymmetric vortices. The size of North Atlantic TCs ranges from 101 km to 370 km (10^{th} - 90^{th} percentile). The radii of maximum winds (RMWs) of North Atlantic TCs have a 10^{th} - 90^{th} percentile range of 28 km to 111 km (Chan and Chan, 2012). The deviation from a perfect circular vortex is often measured by an asymmetry index (AI), which synthesizes measured radii in each quadrant around the TCs center (Chan et al., 2023). Chan et al. (2023) analyzed AIs of different sizes and found that TCs are rarely symmetric in all basins and highlighted the limitation of taking azimuthal average wind fields to quantify storm sizes.

When investigating physical processes within a TC group for understanding the storm's development and hazards, misaligning eyewall and TC borders brings the drawback of loosing information about processes highly linked to these vortex structures. RMW is often an approximation of the eyewall location (Kepert, 2010; Qin et al., 2016). In the eyewall, strong convection and cloud microphysics provide insights about the secondary circulation and the warm core formation (Kepert, 2010; Smith, 2024; Ohno and Satoh, 2015). Within the vortex, enhanced moist entropy, measured by the equivalent potential temperature (θ_e), provides static instability for the eyewall convection, supports cyclone deepening and is found to increase for intensifying storms (Holland, 1997; Dolling and Barnes, 2012; Juračić and Raymond, 2016). Rainbands are mainly found within and around the vortex border, often defined as the radius where the wind field reaches 17 $\mathrm{m\,s^{-1}}$ (R17) (Kepert, 2010; Chan and Chan, 2012;

https://doi.org/10.5194/egusphere-2025-6186
Preprint. Discussion started: 2 February 2026

Judt et al., 2021). Also most of the precipitation falls withing R17 (Yu et al., 2023). Some studies suggest competing effects of rainband and eyewall convection due to aerosol-cloud interactions in TCs (Lin et al., 2023; Wang et al., 2014; Rosenfeld et al., 2012), which gives another reason to preserve both, eyewall and outer rainbands, as well as make them distinguishable from each other. Besides analyzing features linked to the vortex structure, size, RMW and AI themselves can be useful parameters in studying the evolution of storms and their impact on coastal regions: determining the precise size of a TC can improve the estimation of its destructiveness potential (Emanuel, 1999). RMW is observed to contract during TC intensification due to absolute angular momentum convergence by the overturning circulation, and can coincide with or precede rapid intensification (Stern et al., 2015; Qin et al., 2016), an ongoing challenge in TC forecasting (Zhang and Tao, 2013). Relatively symmetric storms also have larger intensification rates, likely due to the absence of VWS (Li and Tang, 2025). Moreover, symmetric eyewalls can benefit intensification, since they are associated with higher convective organization and larger radial heating gradients (Martinez et al., 2022; Persing et al., 2013).

Some studies tackle the challenge of various vortex structures partially by scaling the storm distances by RMW. These composite methods (Wei et al., 2025; Klotz and Jiang, 2017; Sun et al., 2019; Ming et al., 2015) allow the alignment of eyewalls, within the compositing storm group. Nevertheless, the various vortex sizes and asymmetries are not considered in such an approach.

This study presents a novel approach to composite TCs addressing their large spread in vortex sizes and axis-asymmetries: the SYmmetrized-Normalized Cyclone (SyNC) composite framework aims to symmetrize TCs to axisymmetric storms and normalize them according to their eyewall location and storm border to preserve the individual storm structures and associated features when compositing cyclone groups with various asymmetries and sizes. It further presents an approach to accurately detect the vortex and eyewall sizes, as well as corresponding axis-asymmetries. We developed the method on a group of numerically simulated TCs and compare their characteristics and structure to observations.

https://doi.org/10.5194/egusphere-2025-6186
Preprint. Discussion started: 2 February 2026

2 Methods

2.1 Model setup

For the development and demonstration of the SyNC composites, the North Atlantic TC season 2005 was simulated using the non-hydrostatic numerical weather prediction and climate model ICON (2024.10) (Zängl et al., 2015) in limited area mode. The model domain spans the North Atlantic ocean (5° N to 45° N, 105° E to 18° E) using a triangular grid with 5 km (grid R2B9, with a mean effective resolution of 4.9 km and a minimum / maximum effective resolution of 4.0 km / 5.0 km, respectively) horizontal resolution, 80 vertical levels up to 23 km and a time step of 25 s. Initial and six-hourly boundary conditions were taken from ECMWF IFS HRES data. Sea surface temperature was prescribed using daily interpolated monthly means. Simulations ran from 01.07.2005 to 01.12.2005, including a two week spin-up. The model physics is represented by a set of parametrisations: the prognostic turbulent kinetic energy (TKE) scheme for turbulences (Raschendorfer, 2001), the ecRad scheme for radiation (Hogan and Bozzo, 2018) , the TERRA scheme for land surface processes (Schulz et al., 2016) and the two-moment scheme of Seifert and Beheng (2006) for clouds, predicting mass and number concentrations of cloud droplets, ice crystals, rain, snow, graupel and hail. Cloud droplet's growth is implemented by saturation adjustment, whereof they are formed by the cloud condensation nuclei (CCN) activation scheme of Segal and Khain (2006). The CCN concentration is prescribed to 500 cm^{-3} representing average conditions over the North Atlantic (Choudhury and Tesche, 2023). Deep and shallow convection parametrisations are switched off to align our setup with convection-permitting ICON studies from Hohenegger et al. (2023), Weiss et al. (2025) and Segura et al. (2025). Hohenegger et al. (2020) showed, that ICON is able to sufficiently capture the water and energy budgets, the cloud distribution in the tropics and the location of the InterTropical Convergence Zone (ITCZ) and hence is able to reproduce key features of the climate system without convection parametrisations at 5 km. Additionally, Judt et al. (2021) demonstrated that both simulated TC numbers and Accumulated Cyclone Energy (ACE) in ICON are much closer to observational values when the deep convection parametrization is switched off.

An ensemble of 8 members was computed to increase the TC group size and assess the internal variability in the simulations. Ensemble members were created according to the method described by Fischer et al. (2023) by perturbing the initial specific moisture field. Random perturbations on the order of a rounding error ($\pm 10^{-13}$ $\mathrm{kg\,kg^{-1}}$) were added to the initial moisture field. The initially small perturbations grew as the simulations proceeded. The resulting member spread enables the coverage of plausible variants of the simulated storms.

2.2 TC tracking

TCs were identified using the multi-parameter TC tracking algorithm of Enz et al. (2023). The algorithm employs three typical TC characteristics: a pressure depression, a cyclonic wind field and a warm core located in the upper troposphere (Kepert and Chan, 2010). The pressure depression is identified by searching a local minimum in the sea level pressure field (p_{min}) and the cyclonic wind field is detected by the vertical component of the relative vorticity field (ζ_{min}). The amplitude of the warm core is identified by an upper-level temperature anomaly (ΔT_{core}). To account for a vertical tilt of the TC, the distance of the upper-level temperature anomaly to the pressure depression (T_{dist}) is also measured. For each of these four parameters multiple threshold values were distinguished. Weak / strong constraints of the thresholds detect weak / strong TCs, respectively. Once a TC center is identified at time step t_0, it is linked to the nearest TC center found at t_{-1}, whereby a maximum translation velocity threshold of 25 $\mathrm{m\,s^{-1}}$ is applied (for more detail see Enz et al. (2023)).

2.3 TC filtering and time normalization

After cyclone detection, simulated TCs were filtered to exclude weak and short-lived systems based on the following criteria: minimum lifetime of 48 h and reaching a minimum central pressure ($\mathrm{p_{min}}$) of 990 hPa or lower. We employed the pressure based intensity scale by Klotzbach et al. (2020), which covers pressure categories ($\mathrm{cat_{pres}}$) from 1-5 starting at a pressure of $\leq$ 990 hPa being $\mathrm{cat_{pres}}$ of 1. The pressure based intensity scale has multiple benefits: pressure measurements are more accurate than wind measurements, $\mathrm{p_{min}}$ is a strong indicator of potential damage (Klotzbach et al., 2020) and the climatological spread in pressure distribution is better captured by numerical models than for maximum winds (Knutson et al., 2015; Bourdin et al., 2024). The wind-pressure relationship of TCs is poorly represented in numerical models often revealing too weak winds for a given central pressure with increasing error towards intense TCs (Bourdin et al., 2024; Judt et al., 2021; Knutson et al., 2015; Reed et al., 2015; Bao et al., 2012). Possible reasons are the sensitivity of the wind-pressure relationship to the model dynamic core (Reed et al., 2015) and the model's physics parametrization, which determine the surface drag in the boundary layer and diabatic heating through cloud processes and by that influence the simulated TC intensities and structures (Bao et al., 2012). Accordingly, pressure-based metrics are more robust and well-suited for analyzing TC activity in numerical models, as demonstrated in the study by Bourdin et al. (2024).

After filtering, the remaining simulated TCs ($\mathrm{cat_{pres}} \geq 1$) are validated by comparing their characteristics with observed cyclones from the HURDAT2 dataset (Landsea and Franklin, 2013). HURDAT2 is a post-storm data reanalysis of satellite, aircraft and weather station measurements and provides best estimates of North Atlantic TC tracks, central pressure and peak winds. To be consistent, observed TCs were filtered with the same criteria as the simulated TCs regarding their lifetime and minimum pressure.

To enable meaningful comparisons between TCs with different lifetimes, the evolution of each storm is normalized, inspired by the method of Schemm et al. (2018). The time axis is rescaled to an interval of [0, 1], where $\mathrm{t_{norm}} = 0$ corresponds to genesis, $\mathrm{t_{norm}} = 0.5$ to the time of minimum central pressure (i.e., maximum intensity), and $\mathrm{t_{norm}} = 1$ to storm lysis. Between these three fix points, the normalized time axis is linearly interpolated to the tracking time steps. Accordingly, the intensification phase spans from $\mathrm{t_{norm}} \in [0, 0.5]$ and the decay phase from $\mathrm{t_{norm}} \in [0.5, 1]$.

2.4 SyNC: Symmetrized-Normalized Cyclone composites

The goal of the SYmmetrized-Normalized cyclone (SyNC) composite approach is to reduce composite blurring from misaligned vortex structures. Each TC is transformed to an axisymmetric vortex and spatially normalized based on the eyewall radius and the storm size. That way, eyewalls and storm borders are aligned when compositing the symmetrized-normalized TCs. In the following, we demonstrate that SyNC sharpens the composite fields, enables an accurate analysis of eyewall processes and helps to distinguish between processes in the inner and outer region of a TC composite even if the TC sizes, structures or vortex asymmetries vary within the cyclone group (Sect. 6.1). SyNC also increases the power of statistical tests (Sect. 6.2).

There are four steps to obtain SyNC composites (see Table 1):

1. Cyclone-centered projection of the TC from a sphere to a plane.
2. Sector-wise eyewall and storm border detection.
3. Vortex symmetrization and normalization.
4. Compositing data fields of a TC group.

First, each TC is projected from the Earth's sphere to a plane using a cyclone-centered Lambert azimuthal equal-area projection. This creates a Cartesian grid (x,y,z) with the grid origin located at the cyclone center addressing the irregular spacing of the grid due to the curvature of the Earth. Therefore, the projected grid preserves the true size of a cyclone and enables the comparison of cyclones across different latitudes. The resolution of the projected grid is defined such that it coincides with the effective model resolution (i.e., $\Delta\mathrm{x} = 5\ \mathrm{km}$). Additionally, the model output is reduced to a $1000\ \mathrm{km} \times 1000\ \mathrm{km}$ square around the TC center to facilitate the post-processing. This defines the extent of the data.

Second, the eyewall and the storm's size are detected based on the tangential wind field (see Fig. 1a). The location of the eyewall is approximated by RMW (Kepert, 2010; Qin et al., 2016). The horizontal extent of the TC is defined as the radius where the wind speed reaches $17\ \mathrm{m\,s^{-1}}$ (Kepert, 2010; Chan and Chan, 2012; Judt et al., 2021) (R17, from now referred to as $\mathrm{R_{out}}$). $\mathrm{R_{max}}$ determines the extent of the processed data and is defined by the prior selected data extent of $1000\ \mathrm{km}$. RMW is identified for each vertical level, allowing to account for the eyewall tilt. When the tangential wind becomes anticyclonic at upper-levels, RMW is taken from the last level below, where winds are still cyclonic. $\mathrm{R_{out}}$ is detected from the tangential wind mean between the surface and $2\ \mathrm{km}$. This ensures better representation of the storm size compared to detecting $\mathrm{R_{out}}$ only at a single vertical level. The $2\ \mathrm{km}$ level was selected, since it leads to the largest TC extents and with that conservatively keeps most of the vortex data in the analysis (find more details and a sensitivity experiment in Sect. A1). $\mathrm{R_{out}}$ is maintained for all height levels. Otherwise, the anticyclonic outflow would unrealistically narrow the vortex size at upper-levels. To make the radii detection robust, some additional rules are implemented: RMW is forced to a minimum / maximum of $15\ \mathrm{km}$ / $400\ \mathrm{km}$. $\mathrm{R_{out}}$ is capped at a maximum of $700\ \mathrm{km}$ and a minimum distance of $30\ \mathrm{km}$ between RMW and $\mathrm{R_{out}}$ is implemented to avoid extensive extrapolation of data points in case of a narrow $\mathrm{R_{out}}$-RMW ring. Additionally, to exclude detected extreme radii, detected RMW and $\mathrm{R_{out}}$ are excluded when exceeding $300\ \%$ or $600\ \%$ of the median of this level, respectively, and replaced with a rolling average of radii in their neighboring sectors. These thresholds were selected based on statistics of observed wind radii and $\mathrm{R_{out}}$-RMW distances. During testing of the algorithm, the thresholds were rounded and adjusted to the simulated TC structure in such a way that the thresholds were only applied when physical radius detection would not have been possible without them. The thresholds are especially necessary for obtaining feasible radii in the early stage of a TC, where the vortex structure is less pronounced and above 15 km, where the vortex ends or the anticyclonic outflow complicates the radii detection. For more details about threshold selection and when they are applied see Sect. A3.

The RMW and $\mathrm{R}_{\mathrm{out}}$ detection is done for 10 circle sectors (i.e., 36° sectors) individually around the cyclone center to account for vortex asymmetry (Fig. 1a). The detection resolution of 36° was chosen such that each sector contains at least one grid cell within the detection minimum of RMW (illustrated in Fig. A3b), which is a necessary condition to detect RMW for each sector. Hence, the maximum number of detection sectors is dependent on the data resolution, whereof for higher resolution, also a higher number of detection sectors can be employed. A high number of detection sectors can improve the detection of vortex asymmetries, as shown by a sensitivity experiment of AI to the number of detection sectors (Sect. A2). These findings suggest that the highest feasible number of detection sectors should be selected. The 10 detected $\mathrm{R}_{\mathrm{out}}$ values are smoothed by a rolling mean over 3 data points to avoid spikes in the TC size. After this, the resolution of detected RMW and $\mathrm{R}_{\mathrm{out}}$ is increased by linearly interpolating the detected radii from 36° sectors to 1° sectors (Fig. 1b). This allows for a more continuous vortex normalization in the next step.

The spatial normalization is conducted such that the TC center is located at the grid origin, while the storm's eyewall / edge are forced to a normalized radius of 1 / 8, respectively (Fig. 1b). The normalized radius of 1 and 8 are chosen such that the ratio of RMW to $\mathrm{R}_{\mathrm{out}}$ is approximately preserved. The radial normalization of the cyclone is employed in cylindrical coordinates (x,y,$z \rightarrow r_{true}$, φ_{true}, z). Based on the eyewall and border distance to the origin (r_{true}), a one dimensional linear interpolation function is defined, that transforms the real radius to the unit-less normalized radius (r_{norm}) by assigning RMW a value of 1, $\mathrm{R}_{\mathrm{out}}$ a value of 8 and $\mathrm{R}_{\mathrm{max}}$ a value of 20 ($r_{true} \rightarrow r_{norm}$). Hence, each grid cell of the projected grid obtains a new normalized radius while preserving the angles (r_{true}, φ_{true}, $z \rightarrow r_{norm}$, φ_{true}, z). The normalization is done for each of the 1° sectors individually, which forces any TC to be an approximately axisymmetric vortex. After the radius transformation, any data field (ϕ) can be interpolated from the transformed grid to a normalized grid by applying 2D cubic interpolation (ϕ (r_{norm}, φ_{true}, z) $\rightarrow \phi^{*}$ (r_{norm}, φ_{norm}, z), Fig. 1c). Note that the radius transformation and data interpolation are conducted for each height level, hence the full three dimensional fields of the TCs are symmetrized and normalized. Last, the normalized grid is converted from cylindrical to Cartesian coordinates, from which SyNC composites are calculated.

https://doi.org/10.5194/egusphere-2025-6186
Preprint. Discussion started: 2 February 2026

Table 1. Steps to obtain the symmetrized-normalized TC composites and corresponding coordinate conversions. The geographic coordinate system is defined by the coordinates latitude lat, longitude lon and height z. The cartesian coordinate system spans over the horizontal plane with x and y with the vertical coordinate z. The cylindrical coordinate system is described by the radial distance to the TC center r, the azimuth φ and height z. The subscript $true$ refers to the real cylindrical coordinate system, while the subscript $norm$ indicates the normalized cylindrical coordinate system. ϕ represent any three-dimensional data field of one TC, ϕ^* the data field after interpolation and $\phi^*{}_{\mathrm{mean}}$ the data field mean over a group of cyclones.

	Process	**Coordinates**
1	Lambert azimuthal equal-area coordinate projection	sphere (lat, lon, z) $\longrightarrow$ plane (x, y, z)
2.1	Sector-wise detection of RMW and $\mathrm{R_{out}}$	10 sectors (φ_{true})
2.2	Upscaling of detected RMW and $\mathrm{R_{out}}$ using 1D linear interpolation	10 $\longrightarrow$ 360 sectors (φ_{true})
3.1	Sector-wise radius transformation based on RMW and $\mathrm{R_{out}}$	$(r_{true}, \varphi_{true}, z) \longrightarrow (r_{norm}, \varphi_{true}, z)$ for 360 sectors
3.2	Data interpolation onto normalized grid using 2D cubic interpolation	$\phi\ (r_{norm}, \varphi_{true}, z) \longrightarrow \phi^*\ (r_{norm}, \varphi_{norm}, z)$
3.3	Conversion to Cartesian coordinates	$\phi^*\ (r_{norm}, \varphi_{norm}, z) \longrightarrow \phi^*\ (x_{norm}, y_{norm}, z)$
4	Cyclone compositing	$\phi^*{}_{\mathrm{mean}}\ (x_{norm}, y_{norm}, z)$

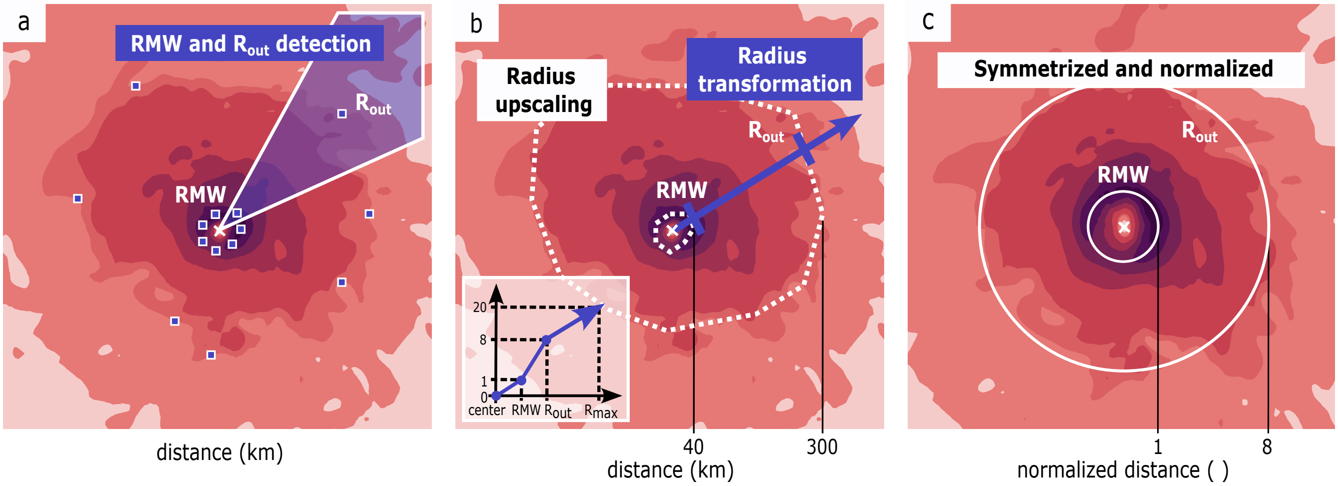

Figure 1. Illustration of the process steps to symmetrize and normalize TCs. Sector-wise RMW and $\mathrm{R_{out}}$ detection (**a**). The purple squares indicate the detected radii, while the purple shaded area highlights one detection sector. Upscaled detected radii (dashed white circles) and sector-wise radius transformation (purple arrow) by a linear function converts real radii to a normalized radii, sketched by the function in the left lower corner of the panel (**b**). A symmetrized-normalized TC on the normalized grid (**c**). The red contours in (**a**)-(**c**) illustrate an exemplary tangential wind field of a TC.

https://doi.org/10.5194/egusphere-2025-6186
Preprint. Discussion started: 2 February 2026

2.5 Asymmetry index

The asymmetry index (AI) is calculated to assess the vortex shapes of the different cyclone groups and to estimate the relevance of the vortex symmetrization. The AI is defined as the ratio of the maximum radius to the effective radius of four quadrants (Chan et al., 2023). Here, we calculate AI for the overall storm using $\mathrm{R_{out}}$ and for the eyewall using RMW. Instead of estimating asymmetry based on four quadrants, all detection sectors $(s1, s2, ...sn)$ are used, such that AI is defined as the following:

$$R_{max} = \max(R_{s1}, R_{s2}, ...R_{sn}) \tag{1}$$

$$R_{eff} = \sqrt{\frac{\sum_{s=1}^{sn} R_s^2}{sn}} \tag{2}$$

$$AI = \frac{R_{max}}{R_{eff}} - 1 \tag{3}$$

where R is the detected $\mathrm{R_{out}}$ or RMW in the tangential wind field for each vertical model level and sn the number of detection sectors. Hence, AI of 0 indicates a perfectly symmetric structure.

2.6 Statistical significance

To assess the significance of differences between cyclone groups, we employ independent two-sided permutation tests. The test statistic is the group mean, with the null hypothesis stating that the means of the cyclone groups are equal. By randomly drawing cyclone fields from the two groups, synthetic cyclone groups are generated. This process is repeated 10,000 times. The distribution of the synthetic group means is then used to estimate the confidence interval for the null hypothesis (Wilks, 2011). The null hypothesis is rejected at a significance level of 0.05.

The permutation tests are conducted for each grid cell in the azimuthally averaged composites. To correct for multiple testing along the radius- and height-axis, and the associated risk of falsely rejecting the null hypothesis (Ventura et al., 2004), we tighten the statistics by controlling the false discovery rate (FDR) at a level of 0.05, applying the method of Benjamini and Hochberg (1995).

3 Simulated TC validation

3.1 Wind-pressure relationship

To evaluate the ICON-simulated TCs, the relationship between simulated wind and central pressure is compared to observations in Fig. 2. For a meaningful wind-pressure relationship comparison, wind and pressure should ideally be diagnosed at the same vertical level. While observations are typically available at $10\ \mathrm{m}$, numerical models often struggle to accurately represent surface winds due to their sensitivity to surface drag parameters and boundary layer parameterizations (Bao et al., 2012). In contrast, simulated central pressure is generally more reliably represented (Judt et al., 2021).

To minimize the influence of surface parameterization, the model level is identified where the wind-pressure relationship aligns best with observations. This provides a wind-based intensity estimate for simulated TCs that is consistent with pressure-based estimates, exploiting the higher confidence in the simulated central pressure. It further enables a comparison of wind magnitudes between model and observations while excluding model biases near the surface.

As expected, a large bias in the simulated wind-pressure relationship occurs near the model surface (Fig. 2). Most simulated $10\ \mathrm{m}$ winds are weaker than observed winds for a given central pressure, and the fitted line suggests a linear relationship, whereas observations clearly indicate a nonlinear one (Fig. 2a). The fit improves at higher altitudes until $0.13\ \mathrm{km}$, where one of the best fits is located with a MSE of only $9\ \mathrm{m}^2\,\mathrm{s}^{-2}$ (Fig. 2c). Above $0.13\ \mathrm{km}$, TC winds appear too strong for given central pressure until $3\ \mathrm{km}$ (Fig. 2d-f), likely due to a typical vortex structure of a TC revealing maximum wind speeds within these low-level altitudes. Between $3\ \mathrm{km}$ and $4\ \mathrm{km}$, the wind-pressure relationship again matches observations relatively well across all wind intensities (Fig. 2g). Above $4\ \mathrm{km}$, the discrepancy between model and observed wind-pressure relationships increases again (Fig. 2h), likely because using surface pressure with winds from higher altitudes becomes an oversimplification, causing the relationship to break down, and winds start to weaken at these altitudes. Therefore, the $0.13\ \mathrm{km}$ level is selected for further comparisons between observed and simulated wind fields, as it offers the best alignment with observations while also being rather close to the surface. Notably, the model reproduces intense stages of TCs accurately, covering the full range of observed winds and pressures, although it slightly under-represents weaker stages (i.e., high central pressures). The lack of weak stages may originate from the TC tracker, which likely struggles to detect the weak and very early stages of TCs (Enz et al., 2023), when the storm's central pressure is close to the ambient pressure. As a result, these stages are potentially missed in our analysis.

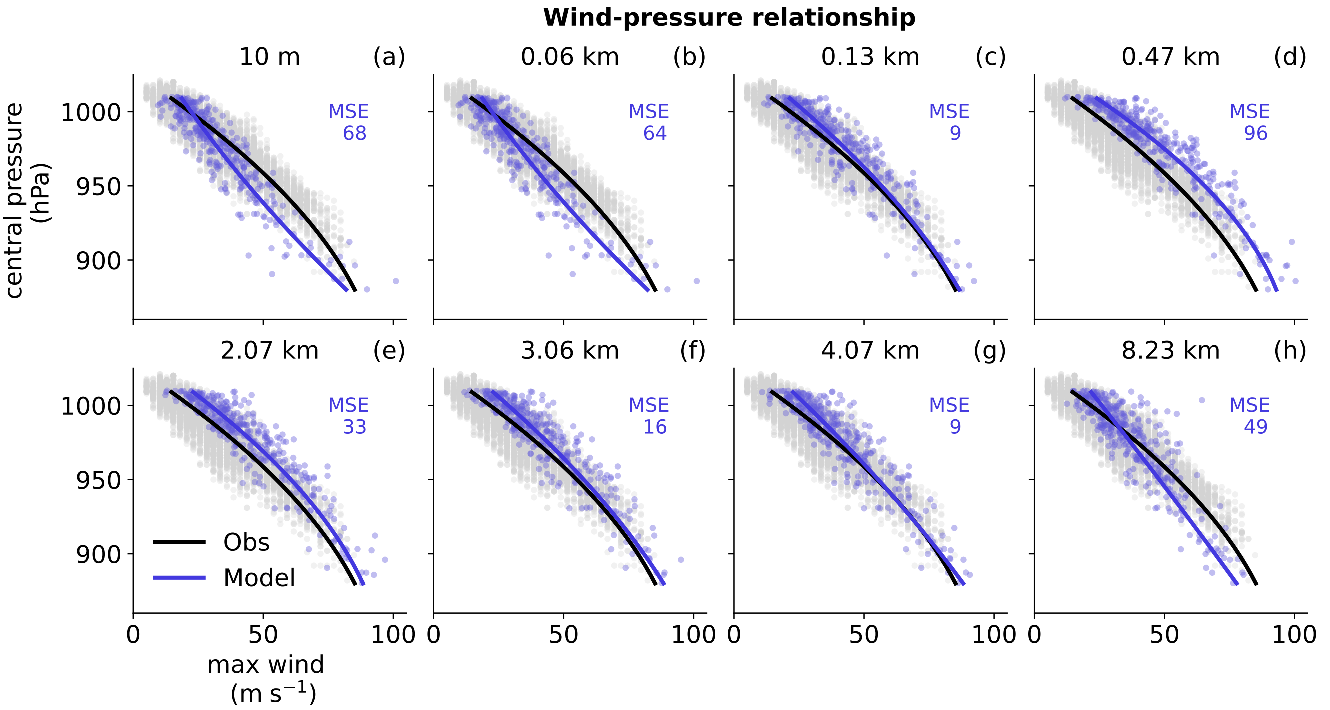

Figure 2. Wind–pressure relationship across TC life cycles for observations (black, n = 12,318) and model output (blue, n = 363). Observed winds are at 10 m, modeled winds are selected from 10 m to 8.23 km (**a**-**h**). Curves show a quadratic fits excluding outliers. The mean squared error (MSE, in $\mathrm{m^2\,s^{-2}}$) of the model fit is indicated in each panel.

3.2 TC characteristics

Simulated TCs are validated against observed North Atlantic TCs using the HURDAT2 dataset (Landsea and Franklin, 2013). Figure 3 presents various TC characteristics derived from the North Atlantic TC climatology (1980-2024, black), the observed hurricane season 2005 (red) and the simulated TCs (blue). Overall, the simulated TC characteristics show good agreement with observations, as indicated by predominantly insignificant differences (gray arrows) between the distributions of most metrics. Simulated TCs predominantly form between August and October, aligning with the observed peak TC activity (Fig. 3h). However, the model fails to generate TCs during the late months of the North Atlantic TC season (November). On average, simulated TCs last approximately eight days (Fig. 3d), with the intensification phase spanning roughly half of their lifetime (Fig. 3l), consistent with observed behavior. The spatial distribution of simulated tracks appears realistic with genesis locations (Fig. 3i) and points of maximum intensity (Fig. 3j) closely matching observations. Nevertheless, simulated termination latitudes are slightly lower than those observed (Fig. 3k), likely due to the model domain being limited to 55° N.

Regarding storm intensity, the model shows a tendency to produce more intense TCs, as indicated by the significantly lower median central pressure median of 938 hPa compared to the climatological median of 968 hPa (Fig. 3e) and a notably higher median maximum winds of 67 $\mathrm{m\,s^{-1}}$ compared to the observed 46 $\mathrm{m\,s^{-1}}$ (Fig. 3f). Simulated TC also intensify more rapidly, with a peak pressure decrease median of -2.3 $\mathrm{hPa\,h^{-1}}$, while observations only show a median of -1.5 $\mathrm{hPa\,h^{-1}}$ (Fig. 3g). This bias towards more intense and rapidly intensifying storms may originate from the model's initiation and forcing using the extremely active North Atlantic TC season of 2005. The hypothesis is supported by the central pressure, wind and pressure decrease distributions of the observed season 2005, which do not show significant differences from the model. Surprisingly, the model is able to reproduce extremely intense systems, which is a well known challenge of numerical models (Judt et al., 2021; Bourdin et al., 2024). However, with a median of only 4 simulated TCs $\mathrm{season^{-1}}$ (Fig. 3a), the model clearly underestimates TC frequency compared to the observed 16 storms in 2005 and the climatological median of 6 TCs $\mathrm{season^{-1}}$. Since the number of major hurricanes is close to observed ones (Fig. 3b), this suggests that the model generates a too high fraction of major TCs, while weaker storms are relatively rare. This is also evident in the distribution of pressure based TC categories: the model generates median $\mathrm{cat_{pres}}$ 4 TCs (Fig. 3c), whereas the climatology and the season 2005 indicate a median $\mathrm{cat_{pres}}$ 2 / $\mathrm{cat_{pres}}$ 1.5, respectively. Thus, the model appears particularly capable of simulating major hurricanes, while still being able to represent the full range of storm intensities among the simulated TCs.

To validate the vortex structure of the simulated TCs, azimuthally averaged wind profiles at maximum intensity are compared between simulated and observed TCs (Fig. 4). The median values of R33, R25, and R17 for the simulated TCs are close to those observed. While the spread of R33 and R25 radii also aligns with observations, the spreads of simulated R17 and RMW are slightly lower. Additionally, the median simulated RMW is smaller than observed values. This suggest that the simulated eyes are somewhat narrower and the vortex structures tend to be slightly more uniform than those observed. Nevertheless, with a relatively good agreement of vortex structures, sizes and TC characteristics between model and observations, the simulated TC group is suitable for testing and demonstrating the SyNC framework.

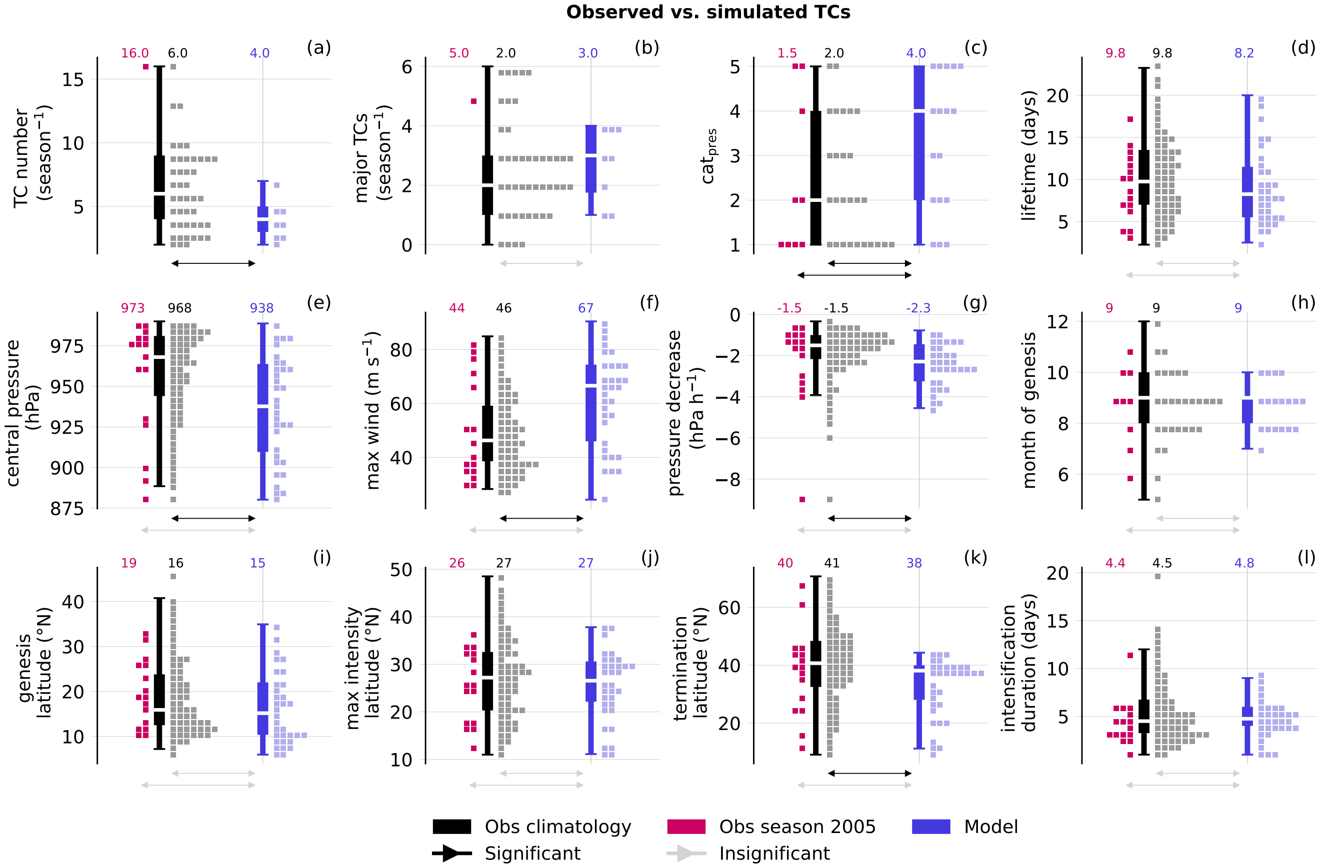

Figure 3. Comparison of observed and simulated TC activity: number of TCs per season (**a**), number of major hurricanes per season (**b**), overall distribution of pressure based categories (**c**), storm lifetime (**d**), minimum central pressure reached (**e**), wind at maximum intensity (**f**), largest pressure decrease within intensification phase (**g**), month of genesis (**h**), latitude of genesis (**i**), latitude of maximum intensity (**j**), latitude of termination (**k**) and intensification duration (**l**). Maximum winds in (**f**) are taken at 10 m for observations and at 130 m for the model. Black box plots show observed climatology (HURDAT2, since 1980), blue box plots show model results. Squares indicate underlying distributions: gray for observed climatology (n = 297, 1 square = 6 TCs), red for observations of the season 2005 (n = 16, 1 square = 1 TC), and blue for the model (n = 33, 1 square = 1 TC). In (**c**), each square represents 2 TCs for the model and the season 2005, and 12 TCs for the climatology for better visibility. Numbers above each panel indicate the distribution medians. Arrows at the bottom denote insignificant (gray) or significant (black) deviations of the model from the observed climatology (short arrow) or from the season 2005 (long arrow) based on a two-sided permutation test at a significance level of 0.05.

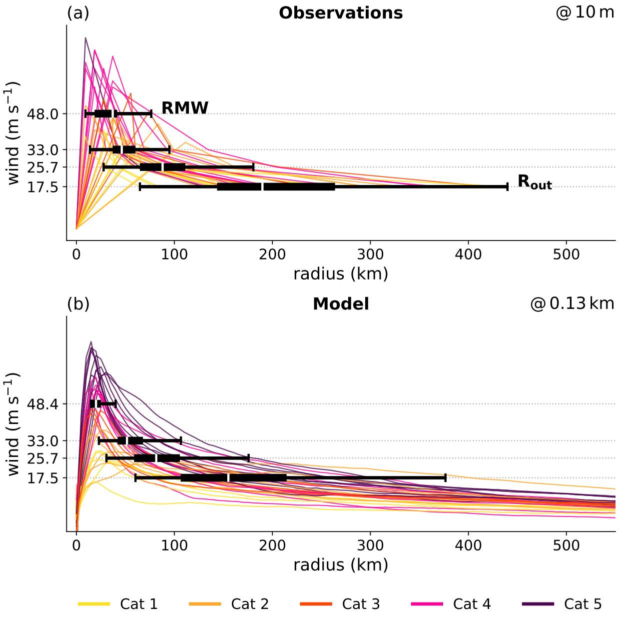

Figure 4. Vortex structures of observed (**a**) and simulated (**b**) TCs at maximum intensity (n = 33 for model and observations). Observed wind radii (at 10 m) are taken from HURDAT2 since 2021, where RMW and R_{out} estimates are available. A zero-velocity point at the center is added for illustration. Simulated winds are azimuthally averaged at 130 m. Box plots show the distribution of commonly used TC wind radii: 17.5 $\mathrm{m\,s^{-1}}$ (34 knots), 25.7 $\mathrm{m\,s^{-1}}$ (50 knots), 33 $\mathrm{m\,s^{-1}}$ (64 knots) and RMW. Lines represent individual TCs, colored by their maximum reached pressure-based category.

4 SyNC case studies

The symmetrization and normalization of two individual TCs is demonstrated in Fig. 5 and Fig. 6. The $\mathrm{cat_{pres}}$ 5 storm (Fig. 5) reveals a typical TC vortex structure, exhibiting a calmer eye, a distinct eyewall and decaying winds at larger distance with an overall asymmetric vortex structure. Before the symmetrization and normalization (Fig. 5c), the tangential wind field is shifted into the northeastern quadrant, likely due to wind shear pushing the vortex towards the northeast typically observed in North Atlantic TCs (Li and Tang, 2025; Klotz and Jiang, 2017) and the storm translation vector aligning with the tangential winds (Uhlhorn et al., 2014). Accordingly, with R_{out} varying from about 150 km to 600 km, AI of R_{out} is found to be 0.36 (Fig. 5a). Also RMW shows asymmetry, with an AI of 0.27 (Fig. 5b). After symmetrization and normalization, the vortex becomes symmetric around the storm center (Fig. 5d). RMW and R_{out} are repositioned to a normalized radius of 1 and 8, respectively. Small-scale features in the data field are preserved, with only their radial distances adjusted while their angular positions relative to the center remain unchanged.

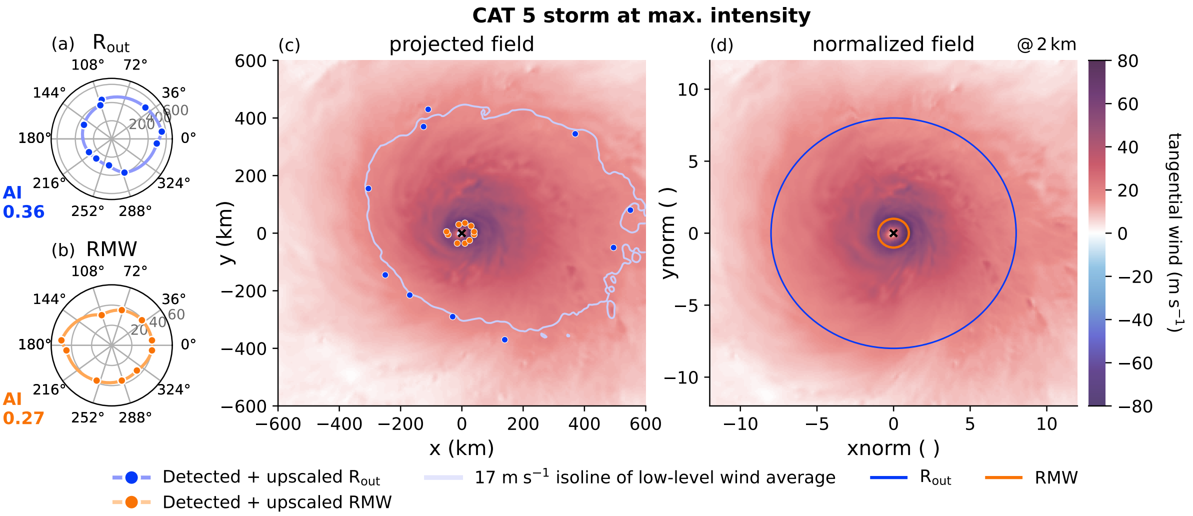

Figure 5. Demonstration of detected wind radii and the effects of SyNC of a cat$_{pres}$ 5 storm at maximum intensity. Detected (blue points) and upscaled (blue line) R$_{out}$ (**a**). Detected (orange points) and upscaled (orange line) RMW (**b**). The asymmetry index (AI) of R$_{out}$ and RMW is noted in the left corner of corresponding sub panel. The vortex on the projected grid (**c**). The cyclone center is marked with a black cross. Contours show the tangential wind field at 2 km height with detected R$_{out}$ (blue points) and detected RMW (orange points). The light blue line marks the 17 $\mathrm{m\,s^{-1}}$ contour of the low-level (0-2 km) tangential wind average used for R$_{out}$ detection. The vortex on the normalized grid (**d**). Contours show the tangential wind field after symmetrization and normalization, where the location of R$_{out}$ (blue circle) and RMW (orange circle) are highlighted.

Symmetrization and normalization are more challenging for less well-organized TCs. A cat$_{pres}$ 1 storm, illustrated in Fig. 6, has not achieved full structural organization. The eyewall of this weaker TC is not completely enclosed within the tangential wind field, and the outer wind distribution remains patchy, with several local wind maxima (Fig. 6c). Despite these irregularities, the algorithm was able to approximate both radii. A notable challenge lies in the cat$_{pres}$ 1 storm's relatively small size and the narrow distance between RMW and R$_{out}$ in the southwestern quadrant. This resulted in extrapolation of data onto the normalized grid, causing a blurring effect in that quadrant (Fig. 6d). Nevertheless, we consider this drawback to be outweighed by the benefit of achieving symmetry in both the eyewall and the storm boundary. Thanks to the relocation process, even this small storm becomes perfectly aligned with the eyewalls and boundaries of the other TCs in the group during composition.

https://doi.org/10.5194/egusphere-2025-6186
Preprint. Discussion started: 2 February 2026

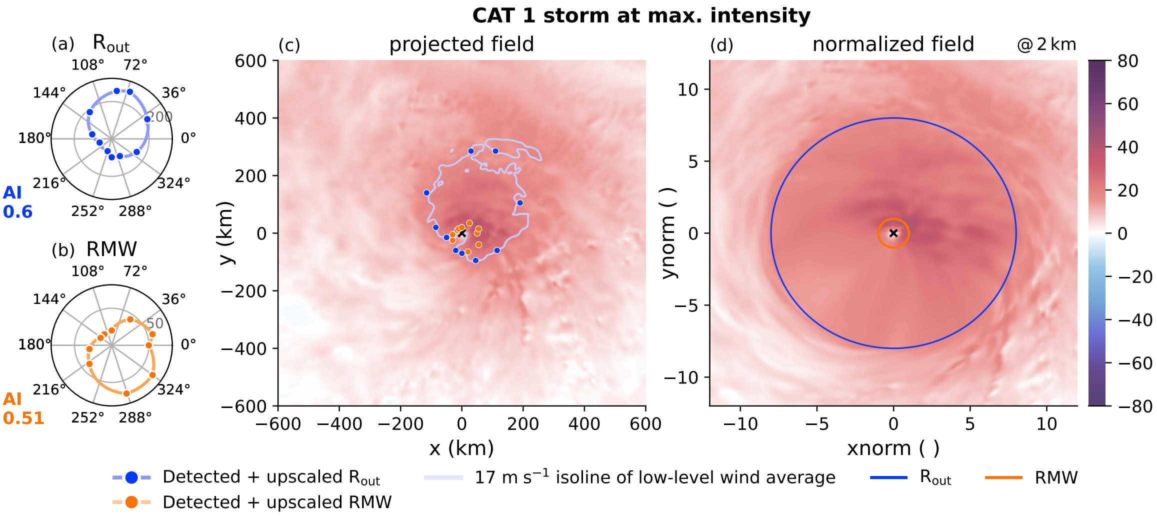

Figure 6. As Fig. 5, but for a cat_{pres} 1 storm.

5 Storm structure evolution

The novel composite method can be used to analyze structure evolution of TCs demonstrated in this section. Fig 7a-c illustrates the vortex structure evolution of observed (black) and simulated (blue) TCs. The model and observations show relatively good agreement in the structure evolution throughout the life cycle. Both observed and simulated TCs exhibit a contraction of RMW during the intensification phase reaching minimum RMWs at peak intensity (Fig 7a), aligning with previous studies (Stern et al., 2015; Qin et al., 2016). The simulated RMW magnitudes generally align well with observations, indicating that the model realistically reproduces eye and eyewall sizes. R_{out} values slightly increase in the decay phase in both datasets (Fig 7b). However, simulated R_{out} values are consistently overestimated due to systematic differences in the detection method, as discussed in Sect. A1. Also, both simulated radii are significantly larger than observed values near and shortly after genesis, likely because tangential wind based radii detection is particularly challenging at that stage. Storm size AIs remain relatively constant throughout the life cycle in both observations and simulations (Fig 7c). Average AI values are approximately 0.4 for simulated TCs and 0.2 for observed TCs, both with spreads of 0.2. The non-zero AI values confirm that axisymmetry is not present in either dataset, as expected. As discussed in Sect. A2, the higher number of detection sectors in the model likely leads to systematically higher AI values in simulations compared to observations. Both observed and simulated TC groups exhibit substantial within-group variability in vortex structure over the life cycle. In the early stage, the IQR of RMW spans approximately 200 km for simulations and 50 km for observations. In the late stage, model and observations show an IQR of around 100 km. The IQR of R_{out} remains around 100 km for both datasets throughout the life cycle. These wide spreads in radii and AI highlight the large diversity in vortex structures within both datasets. This underlines the importance of SyNC to precisely align vortex structures for composite analysis.

Since Li and Tang (2025) found that weaker TCs typically show higher size asymmetries than intense ones, we analyze the vortex structure evolution for storms separately according to their maximum pressure category, as illustrated in Fig. 7d-i for simulated TCs. The storm size and size asymmetry are both not significantly changing between the various storm intensities in the model (Fig 7e, f), contradicting results of Li and Tang (2025). On the contrary, the eyewall evolution shows distinguishable differences between weak and strong TCs (Fig. 7d). While all storm categories indicate the RMW contraction, it is much more pronounced for cat_{pres} 4 and 5 TCs, which produce the smallest eyewall radii. At maximum intensity, the eyewall radii of intense TCs are significantly smaller throughout all vertical levels than of weak ones. Intense TCs also indicate a smaller vertical gradient in RMW and more symmetric eyewalls throughout the vortex than weak TCs (Fig. 7h-i). At an early stage of the life cycle, RMW AIs start at relatively high values around 0.5 for all TC categories (Fig. 7g). The asymmetry of the eyewall remains at high levels also for weak TCs. However, intense TCs reveal a symmetrization of their RMW during the second half of their intensification phase, when AI drops approximately from 0.4 to 0.2. This is in agreement with previous studies (Persing et al., 2013; Martinez et al., 2022), which found that eyewall symmetrization and associated convective organization is beneficial for TC intensification.

https://doi.org/10.5194/egusphere-2025-6186
Preprint. Discussion started: 2 February 2026

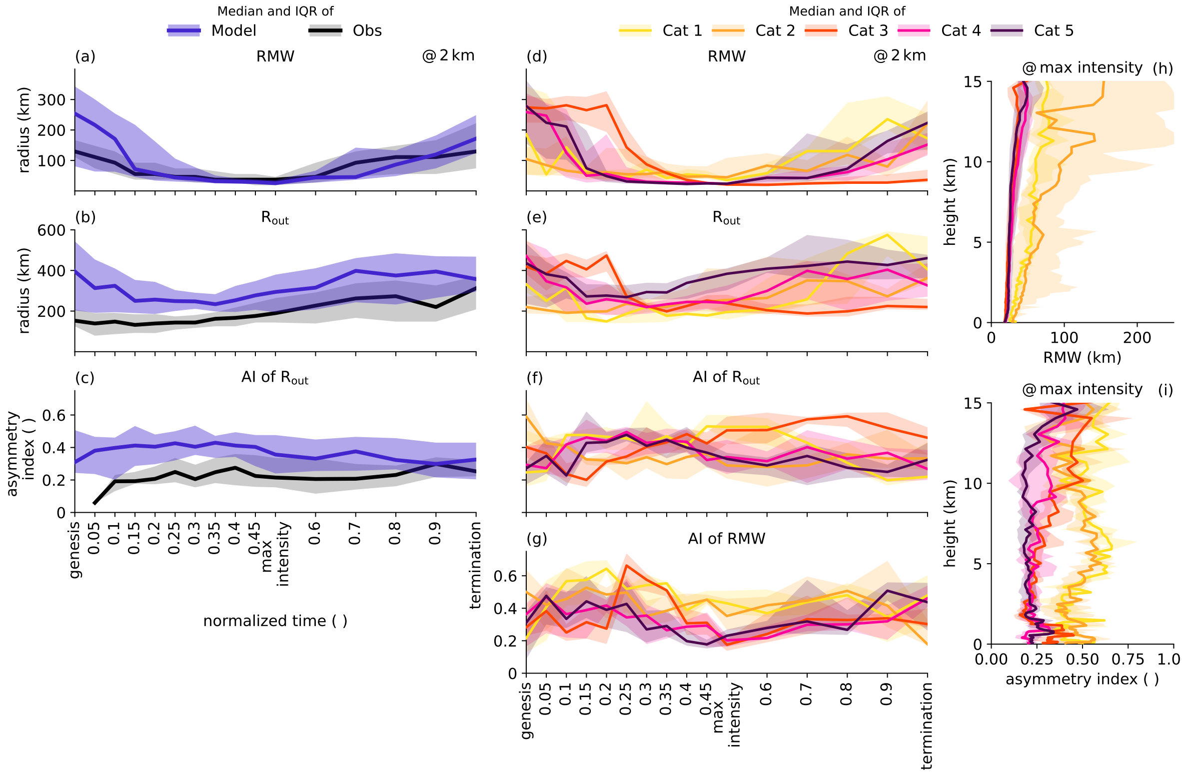

Figure 7. Evolution of TC structure related metrics over the storm's life cycle: RMW (**a**, **d**), R_{out} (**b**, **e**), asymmetry index (AI) of R_{out} (**c**, **f**) and AI of RMW (**g**). Panels (**a-c**) show a comparison of observed TC structures (black) and simulated TC structures (blue). Simulated TC wind radii and AIs are diagnosed at 2 km altitude, observations correspond to 10 m altitude. Panels (**d-i**) show simulated TCs split according to their intensity category. Vertical profiles of RMW (**h**) and RMW AI (**i**) are displayed at maximum intensity. Lines display the group's median and the shaded area represents the interquartile ranges (IQRs). Normalized time ticks indicate the frequency of diagnosed radii and AIs setting a focus on the intensification phase.

6 Composite sharpening by SyNC

6.1 Preserved small features

Simulated TCs were split into weak (cat_{pres} 1-3) and intense (cat_{pres} 4-5) TC groups to evaluate the performance of the composite method and to detect systematic differences between differently intense TCs. These groupings were chosen to maximize structural variability within the weak TC group and minimize it within the intense group based on the results shown in Fig. 7. This design enables an assessment of which TC group benefits most from the SyNC approach, the structural more homogeneous (intense) or more inhomogeneous (weak) group. The cyclone groups were composed by either aligning the storm centers (centered-only) or by the SyNC approach. A comparison of the two composite methods of the intense group can be found in

Fig. 8 (and additional data fields in Fig. C1). Overall, the SyNC composite fields often reveal more pronounced extreme values in the vertical cross sections (positive and negative) compared to the centered-only composites, as illustrated by the probability distribution functions (PDFs) of respective fields (Fig. 8c, f, i and l). The enhanced extremes are attributed to improved alignment of vortex structures and associated storm features, which helps preserve these characteristics more effectively in the group average. Most fields show substantial improvement due to the SyNC method's alignment of the eyewall: Vertical winds indicate stronger eyewall updrafts and stronger downdrafts within the eye (Fig. 8b). Temperature tendencies of the cloud microphysical scheme reveal approximately 10 $\mathrm{K\,h^{-1}}$ higher latent heating within the eyewall (Fig. 8e). Additionally, stronger cooling (evaporative cooling of rain and ice melting), is more distinctly positioned on the inner and outer flanks of the eyewall updraft. Cloud water and precipitation (Fig. C1e and h) also show extended maxima within the eyewall. The super-gradient outflow above the boundary layer (Fig. 8h) is sharpened in the SyNC composite. Tangential winds not only show a larger peak near the eyewall in the lower atmosphere (Fig. 8k), but also indicate stronger winds throughout the vortex due to a better alignment of the vortex borders. The border alignment avoids overlaying environmental and storm regions, which also benefits the equivalent potential temperature field (Fig. C1k). The SyNC composite maintains a higher θ_e especially in the storm's outer region. However, due to the relatively uniform radial nature of the θ_e field, it gains the least from the SyNC compositing. A similar behavior is found for water vapor and longwave radiative cooling, both of which are also radially uniform (Fig. C1n and q).

Similar results are found for the weak storms (Fig. C2 and C3), which are structurally even more variable than the intense one. It is worth mentioning that due to the large variability of eyewall radii in the weak group, secondary peaks in updraft (Fig. C2a) or latent heating (Fig. 10a) may be misinterpreted as features of outer rainbands. However, the SyNC composite clarifies that these are indeed eyewall features.

To statistically quantify the impact of the SyNC compositing method, the Kolmogorov–Smirnov (KS) test statistic is calculated for each variable, measuring the distance between the PDFs of the centered-only and SyNC composite fields (Fig. 8c, f, i and l). Overall, KS statistics of the weak group are comparable to or higher than those of the intense group, suggesting that the weak group benefits slightly more from the SyNC approach. Nevertheless, with overall KS statistics of around 0.1 and larger extreme values, the SyNC method successfully sharpens the composite fields of both, weak (i.e., structurally varying) and intense (i.e., structurally more uniform) cyclone groups.

https://doi.org/10.5194/egusphere-2025-6186
Preprint. Discussion started: 2 February 2026

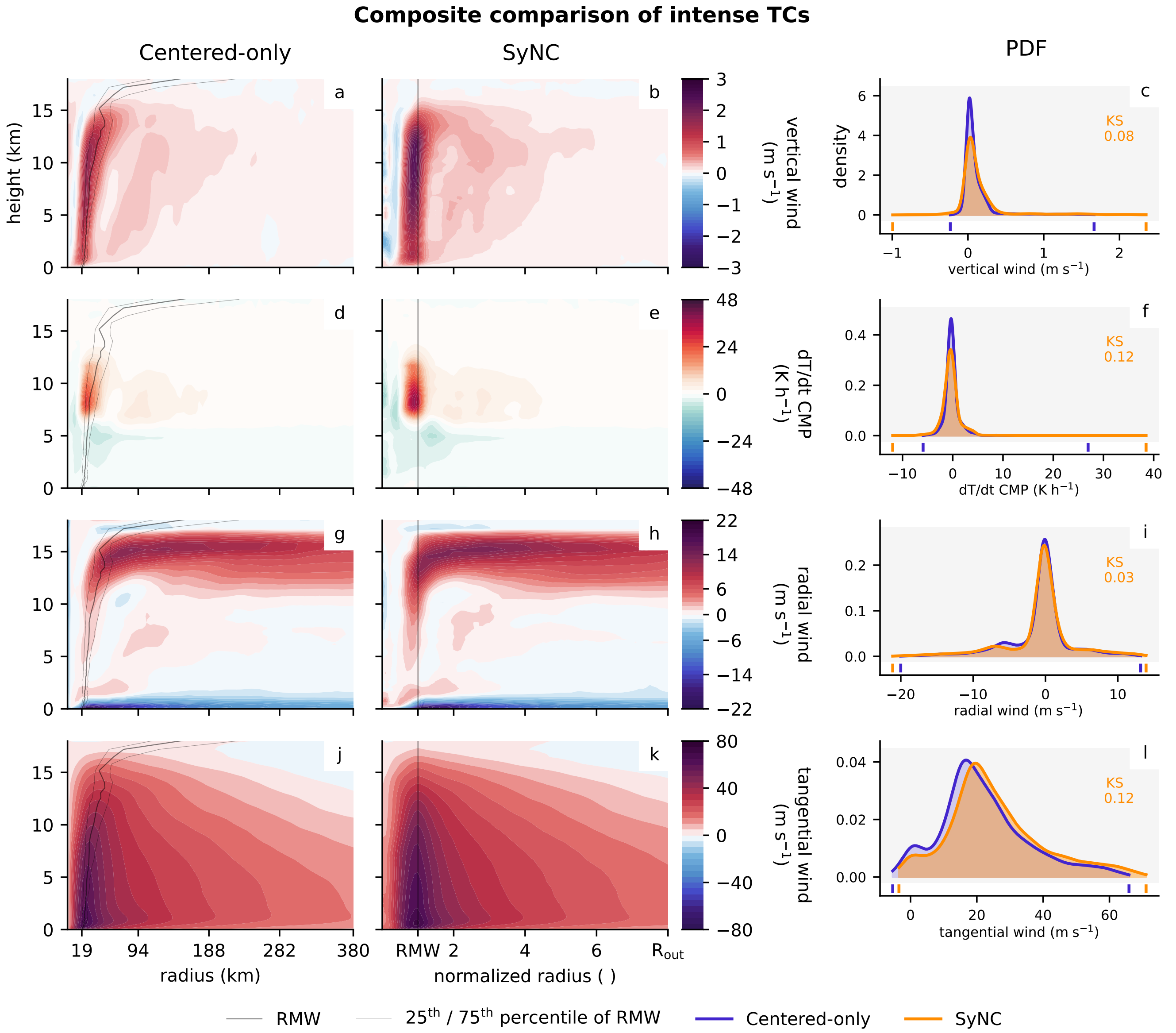

Figure 8. Comparison of centered-only (**a**, **d**, **g**, **j**) and SyNC composites (**b**, **e**, **h**, **k**) of the intense TC group, showing the azimuthally averaged cross sections of vertical wind (**a**, **b**), temperature tendencies from the cloud microphysical scheme (dT/dt CMP, **d** and **e**), radial winds (**g**, **h**) and tangential wind (**j**, **k**). The extent of the cross sections is set to the average R_{out} detected over the TC group. RMW is indicated with a black line, whereof the spread of the eyewall location is shown by the two gray lines for the centered-only approach. Panels (**c**), (**f**), (**i**) and (**l**) show the probability distribution functions (PDFs) of the cross section data fields of the centered-only (blue) and the SyNC (orange) composite methods. Minima and maxima of the PDFs are illustrated by blue/orange ticks on the x-axis. The Kolmogorov–Smirnov (KS) test statistic between the two distributions is noted in each sub panel.

https://doi.org/10.5194/egusphere-2025-6186
Preprint. Discussion started: 2 February 2026

6.2 Enhanced statistical power

The composite sharpening achieved through SyNC compositing can enhance the sensitivity of the statistical testing between two cyclone groups. Figures 9 and 10 display the radial wind and temperature tendencies due to saturation adjustment for both the weak and intense TC group, along with their differences. Statistically significant differences between the two groups are determined via a false-discovery rate corrected permutation test at a 0.05 significance level and are indicated by the hatched areas (Fig. 9i, j and Fig. 10i, j). Interestingly, the regions of significant change differ between the two compositing methods, although the underlying cyclone groups are identical. While the centered-only composite shows the most prominent differences in radial winds, it misses several smaller-scale features that are detected by the SyNC composite (Fig. 9j): Significantly stronger super-gradient outflow above the boundary layer, significantly stronger inflow throughout the vortex and significantly stronger mid-level outflow, potentially induced by rainbands, for intense TCs. There are two main reasons for these differences in detected significance. First, the SyNC composite better aligns the vortex and their small-scale features, which can amplify the observed differences between the two groups, as shown in Fig. 9j and 10j. Second, the vortex alignment can reduce the data spread within a TC group, thereby improving the statistical power of the statistical test (Krzywinski and Altman, 2014). The within-group spread of radial wind is illustrated by the IQR cross sections of each TC group per composite method in Fig. 9c, d, g, h and k. Radial wind IQRs of weak TCs are relatively similar between the composite methods. On the contrary, the intense TCs exhibit a large IQR in the centered-only composite around the eyewall, which is nearly twice that of the intense SyNC composite. To illustrate the impact of the large IQR on the power of the statistical test, box plots (Fig. 9k) show the radial wind distributions of all TCs at a selected grid cell (black star) for both composite methods. For the radial wind, the selected grid cell is located at low levels at the inner side of the eyewall, where super-gradient outflow is forming. First, the box plot medians of two cyclone groups are slightly more apart in the SyNC composite than in the centered-only composite. Second, the IQR of the centered-only intense TCs is larger than for the SyNC composite, spreading from negative (inward) to positive (outward) radial winds. This large IQR likely is a result of the their distinct though slightly displaced eyewalls: At the selected grid cell, inflow is observed for TCs with more narrow eyewalls, while for others already super gradient wind is formed at this distance. The resulting large within-group spread in the data causes the storm group distributions to overlap much more for the centered-only composite than for the SyNC composite, which increases the p-value of statistical testing for the centered-only composite. The eyewall alignment of the SyNC composite results in only outward radial winds at selected grid cells narrowing the within-group spread and reducing the p-value allowing for the detection of a significant difference between the TC groups with the SyNC approach. In the temperature tendency composites (Fig. 10), the centered-only method even fails to detect any significant changes, whereas the SyNC method reveals significantly enhanced latent heating in the intense storms, as expected. In this data field, the differences between the groups are similar for both composite methods (Fig. 10i-j) or at selected grid cells within the eyewall even slightly smaller for the SyNC composite (Fig. 10k). Accordingly, especially the weak group benefits from the eyewall alignment resulting in the amplification of the heating signal there producing smaller median differences between the weak and intense TC groups. However, the within-group variance reduction of the intense TCs by the SyNC composite increases the sensitivity of the statistical testing, outweighing the smaller median differences, and hence detecting a significant difference between the two groups. Thus, by mitigating small eyewall displacements and reducing within-group variance, the SyNC composite proves valuable even for relatively well-organized, more homogeneously structured TC groups, increasing the accuracy of statistical analyses.

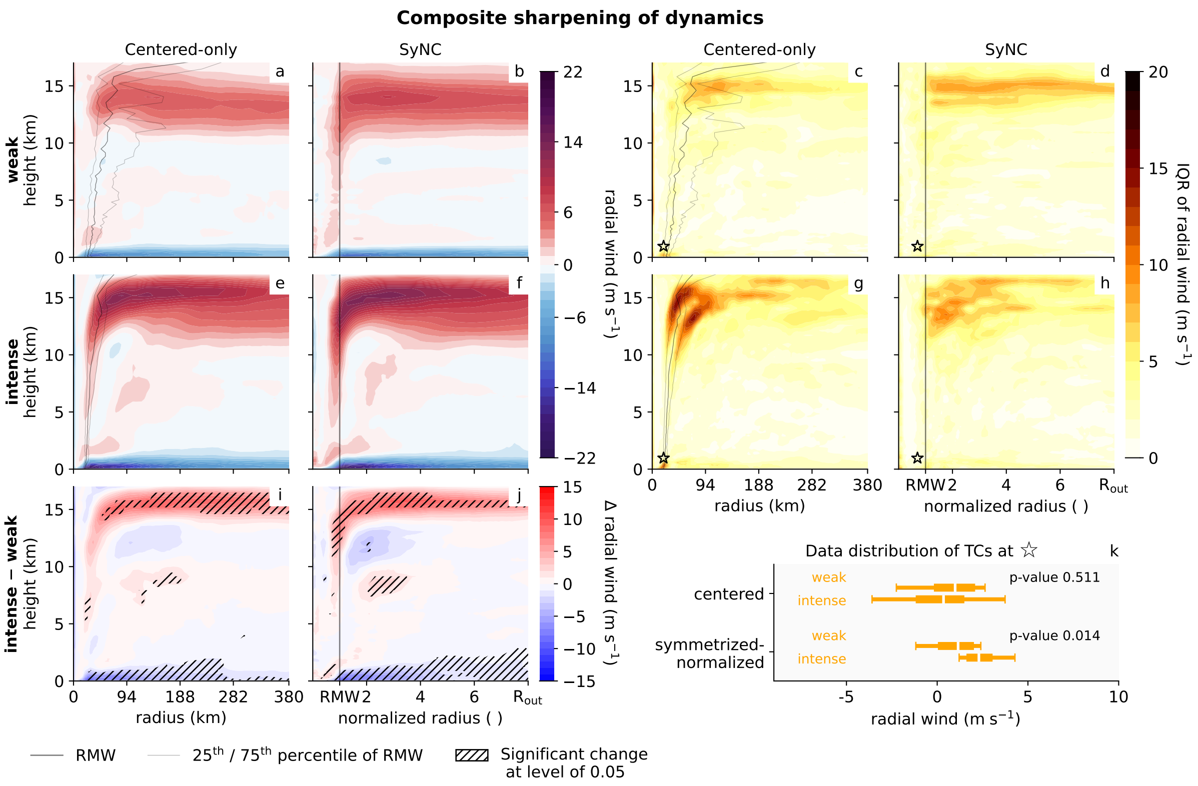

Figure 9. Composite sharpening of radial winds and its influence on statistic testing between weak and intense TC groups: The centered-only composite (**a**, **e**, **i**) of weak TCs (**a**), intense TCs (**e**) and their difference (**i**). Panels (**b**), (**f**) and (**j**) show the same, but for the SyNC composite. Hatched areas (**i**, **j**) indicate statistically significant differences between the two TC groups based on a false-discovery rate corrected permutation test at a 0.05 significance level. The interquartile ranges (IQRs) of each grid cell of both composite methods are shown in (**c**), (**d**), (**g**) and (**h**): centered-only weak (**c**), centered-only intense (**g**), SyNC weak (**d**) and SyNC intense TCs (**h**). The black star highlights one selected grid cell, at which location the data distribution of the TC groups is displayed in (**k**). The p-value at the selected grid cell is indicated within the sub panel (**k**). For the centered-only cross sections, the extent of the cross sections is set to the average R_{out} detected over the intense TC group, since the mean R_{out} of the weak TC group is smaller. RMW is indicated with a black line, whereof the spread of the eyewall location is shown by the two gray lines.

https://doi.org/10.5194/egusphere-2025-6186
Preprint. Discussion started: 2 February 2026

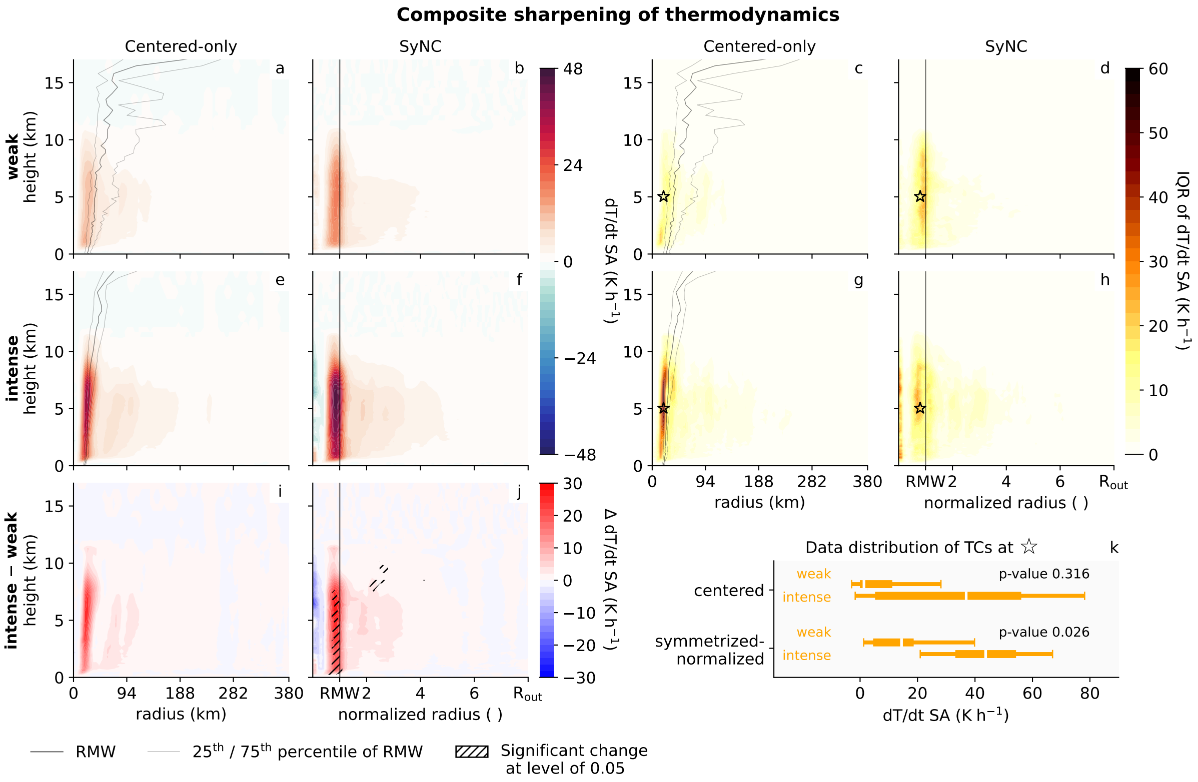

Figure 10. As Fig. 9, but for temperature tendencies due to saturation adjustment (dT/dt SA).

7 Conclusions

We presented the SyNC composite approach, that accounts for TC size and asymmetry, aiming to preserve small-scale features in group composite fields. The symmetrization and normalization process involves sector-wise detection of RMW and R_{out}, followed by a sector-wise radius transformation to a normalized radius and data interpolation onto the normalized grid. SyNC compositing is applied to TCs simulated by ICON, demonstrating strong agreement with observational data in terms of track location, lifetime, and wind–pressure relationship. ICON can generate even the most extreme storms. However, ICON tends to overestimate the frequency of major hurricanes while underestimating the frequency of weaker storms.

The sector-wise detection of RMW and R_{out} enabled by the SyNC approach allows for precise analysis of TC structures. The structural evolution of the simulated TCs reveals eyewall contraction and eyewall symmetrization during intensification, particularly pronounced in intense storms, aligning well with findings from previous studies (Stern et al., 2015; Qin et al., 2016; Martinez et al., 2022; Persing et al., 2013). Additionally, the structural evolution highlights substantial structural variability and pronounced axis-asymmetries across all storm intensities in both simulated and observed TCs, underscoring the importance of SyNC composites in TC analysis. By aligning the eyewall and vortex boundaries during SyNC compositing, the resulting composite fields are sharpened, as evidenced by higher extreme values in the SyNC composite. This method more accurately captures small-scale features such as super-gradient outflow above the boundary layer, eyewall updrafts, and subsidence within the eye as well as cloud properties and associated diabatic heating and cooling. It also more accurately represents regions at the vortex border improving estimates of tangential winds, outer boundary layer inflows and storm's moist entropy, since less environmental air is averaged into the composite field. Furthermore, it reduces within-group variance. While preserving small-scale features is particularly beneficial for storm groups with diverse shapes, within-group variance reduction is especially advantageous for more uniformly shaped but intense storms, where small displacements of strong signals can significantly increase the group's IQR. Together, preserving small-scale features and reducing within-group variance enhance the power of statistical testing, enabling the detection of differences between storm groups, that would be missed using a centered-only composite approach. However, the SyNC compositing method is less effective for radially uniform fields, such as water vapor or longwave radiative temperature tendencies. It is also less suitable during the early stages of a storm's life cycle, when the vortex is not yet fully developed in the tangential wind field. A further limitation is the need for data interpolation onto the normalized grid, which may lead to extensive extrapolation in small TCs or when RMW and R_{out} are close together. Therefore, a careful definition of the normalized grid is essential. Improvements to the SyNC method could include refining detection strategies during the early life cycle stages and at upper levels, where anticyclonic outflow complicates currently implemented radius detection. For wind shear studies, rotating the field according to the shear vector may offer further enhancements. Despite these limitations, the SyNC compositing method significantly improves the accuracy of TC composites and enables reliability of statistical testing of the overall storm structures and small-scale features by overcoming the challenges of various vortex structures. Although the normalization results in the loss of true spatial distances within the vortex, it offers a cyclone-relative framework that facilitates distinguishing between processes occurring within the eyewall and those in the outer regions of the TC. The sector-wise detection of RMW and R_{out} enables high-precision analysis of vortex asymmetries, storm size, and eyewall structures. As such, the SyNC composite method is well-suited for a wide range of research applications.

Appendix A: SyNC configurations

A1 R_{out} detection layer

The symmetrization and normalization of TCs require a selection of several parameters to avoid unphysical radius detection and to ensure algorithm robustness, especially for atypical storm structures that may occur during the early or late stages of a storm's life cycle or in weak systems. To enhance robustness and better represent storm size, R_{out} is not detected on tangential winds at a single vertical level, but rather on the averaged vertical wind over a thicker layer. This detection layer extends from the lowest model level (approximately 60 m) up to a selected altitude. Various detection layer thicknesses were tested ranging from 130 m to 6 km (Fig. A1, brown to blue box plots) to assess the sensitivity of R_{out} to the choice of the detection layer. Observed R_{out} are included as reference (black). All tested detection layers yield larger R_{out} values than observed ones. However, the model successfully reproduces the spread of observed R_{out}'s at all life cycle stages. For all life cycle stages, R_{out} increases with detection layer thickness up to 2 km, then decreases for thicker layers. This behavior can be attributed to the tangential winds, which typically peak around 2 km altitude. The sensitivity is smallest at the early stage. At maximum intensity and in the late stage, R_{out} can vary by approximately 70 km. Since R_{out} defines the vortex boundary in the SyNC composite, we select the detection layer that yields the largest possible vortex boundary being the layer up to 2 km. This conservative approach maximizes the inclusion of data points, while acknowledging that it introduces a systematic bias when comparing R_{out} to observations.

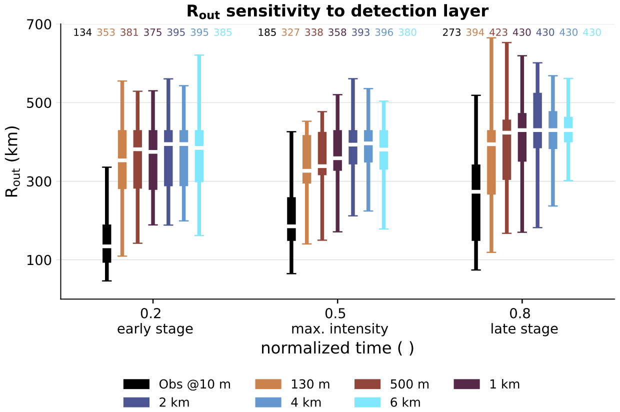

Figure A1. Sensitivity of R_{out} to the detection layer thickness: The colored box plots show the distribution of the detected R_{out} (median over the 10 detection sectors) for all the simulated TCs (n = 33) based on the detection layers reaching from 130 m to 6 km (brown to blue). The black box plots show the distribution of observed R_{out} at 10 m (median over the 4 observation sectors). The sensitivity analysis is performed at three TC life cycle stages: early stage, maximum intensity, and late stage. Box plots medians are indicated above each box plot.

https://doi.org/10.5194/egusphere-2025-6186
Preprint. Discussion started: 2 February 2026

A2 Number of detection sectors

To assess potential benefit of using a large number of detection sectors, we calculated AIs for RMW and R_{out}, based on radii detected in 4, 6, 8, or 10 sectors (Fig. A2, brown to blue). The AI of R_{out} and its spread increase with the number of detection sectors, suggesting that more sectors capture the vortex border asymmetry more accurately. Using only 4 sectors may underestimate AI by about 0.2 to 0.3 throughout the life cycle. Notably, AI of R_{out} is not saturated even with 10 sectors, especially in early stages. Although the 5 km data resolution limits us to a maximum of 10 sectors (Sect. 2.4), using more sectors could further improve AI estimates. Observed AI of R_{out} (black), based on 4 sectors, is slightly higher than the simulated 4-sector AIs of R_{out}. The 6-sector AI of R_{out} aligns well with observations, while 8- and 10-sector AIs exceed them. For RMW, no sector-wise observations are available. Still, simulated AIs of RMW show similar trends: higher AI and greater spread with more sectors at peak intensity. The AI gain from 4 to 10 sectors is about 0.1. Accordingly, RMW AI benefits slightly less from more detection sectors than AIs of R_{out}. At early and late stages, AI appears to saturate between 8 and 10 sectors. Overall, using 10 detection sectors performs best for both radii AI estimates, so we proceed with 10 sectors in this paper.

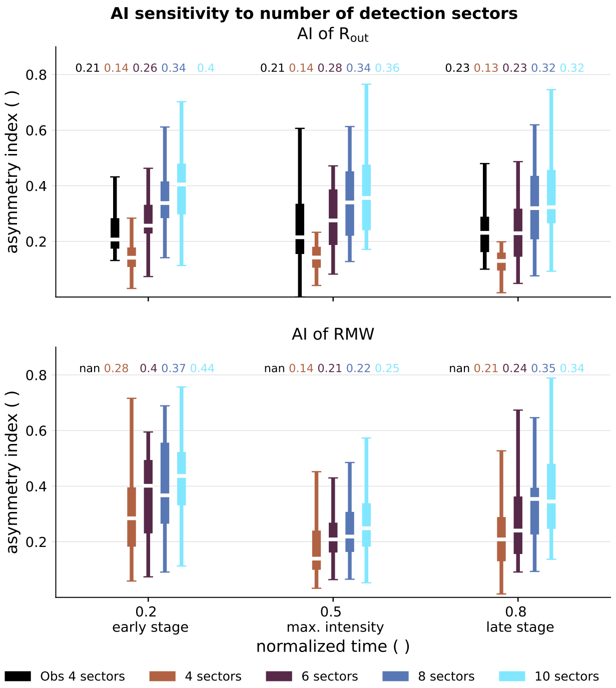

Figure A2. Sensitivity of the asymmetry index (AI) to the number of detection sectors: Colored box plots show the distribution of AIs for all the simulated TCs, where AI is detected based on 4, 6, 8 or 10 detection sectors (brown to blue). The top panel shows AIs of R_{out}, the bottom panel AIs of RMW. The black box plot indicates observed AI of R_{out} based on 4 sectors. No observed RMW AI are available. The sensitivity analysis is performed at three TC life cycle stages: early stage, maximum intensity, and late stage. Box plot medians are indicated above each box plot.

A3 Thresholds

To make the radii detection robust, some thresholds regarding RMW and R_{out} are implemented. Figure A3a shows the observed values for RMW, R_{out} and their difference, which guided the selected minimum thresholds. Figure A3b illustrates the limitation of the data resolution on the selection of number of detection sectors.

Fig. A4, Fig. A5 and Fig. A6 show where and when the six thresholds where applied during detection. The most applied threshold is maximum RMW and minimum distance between RMW and R_{out}. Thresholds where most frequently applied at upper-levels where the tangential wind turned into an anticyclonic rotation and at early and late stages, where the vortex structure is less organized.

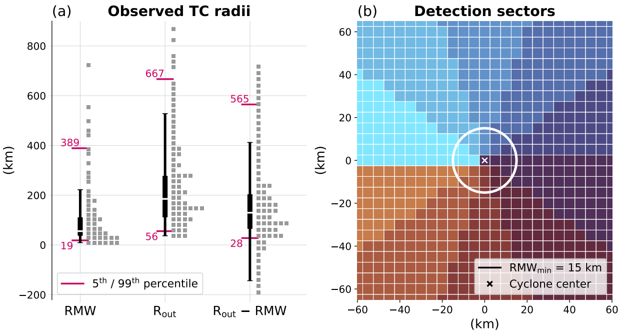

Figure A3. Box plots of observed RMW, R_{out}, and their difference (R_{out}-RMW) over the full life cycle of TCs (**a**), based on HURDAT2 data (since 2021, where RMW and R_{out} estimates are available). Gray squares to the right of each box plot represent 50 / 100 / 100 data points, respectively, to illustrate data distribution. Pink lines mark the 5th and 99th percentiles, asymmetrically chosen in the favor of the larger ones, since ICON tends to produce larger TCs than observed (Judt et al., 2021). For R_{out}-RMW, only positive values were considered to calculate the percentiles due to physical constraints. Schematic of the 10 detection sectors (blue to brown) on a 5 km grid (**b**). The TC center is marked by a white cross and the minimum RMW threshold of 15 km is shown as a white circle.

https://doi.org/10.5194/egusphere-2025-6186
Preprint. Discussion started: 2 February 2026

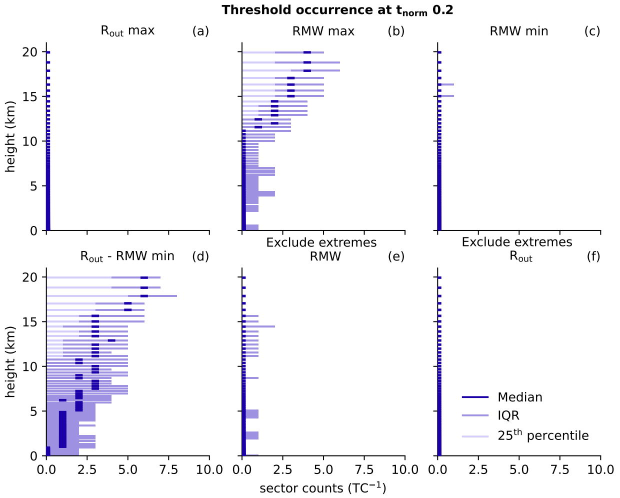

Figure A4. Occurrence of detection thresholds at early stage ($t_{norm} = 0.2$) of a TC: a maximum allowed vortex border R_{out} (**a**), maximum and minimum allowed RMW (**b**, **c**), minimal distance between R_{out} and RMW (**d**). Panels (**e**) and (**f**) indicate occurrences of extremes, which were excluded. For RMW / R_{out} a radius is excluded if it exceeds 300 % / 600 % of the median, respectively. The occurrence is summed over the 10 detection sectors for each TC. The 25th percentile of the counts over all the simulated TCs (light violet), the median (dark violet) and the IQR (medium light violet) are displayed to illustrate the occurrence distribution of the thresholds.

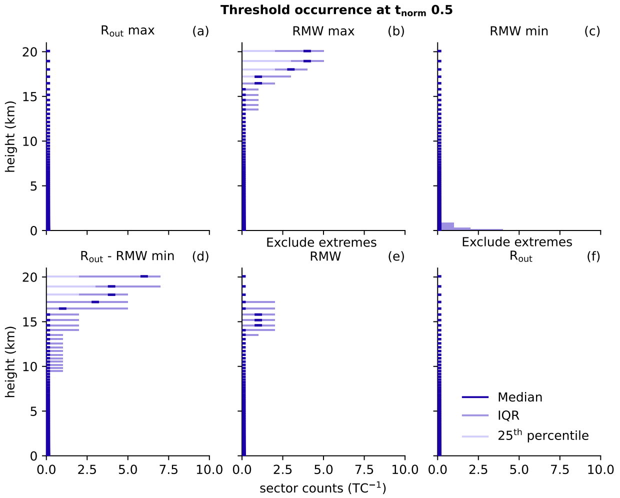

Figure A5. As in Fig. A4, but for maximum intensity ($t_{norm} = 0.5$).

https://doi.org/10.5194/egusphere-2025-6186
Preprint. Discussion started: 2 February 2026

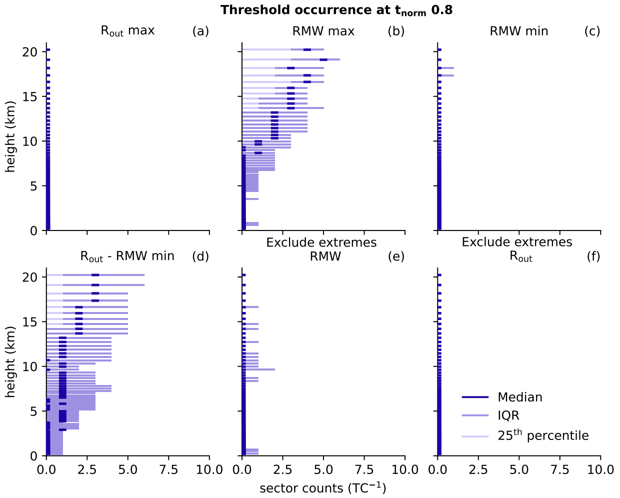

Figure A6. As in Fig. A4, but for a late stage ($t_{norm} = 0.8$).

Appendix B: Unstructured storms

This section provides a few examples of the SyNC composites of less well structured storms. Fig. B1 is the same cat_{pres} 5 TC as in Fig. 5, but at a moment briefly after storm genesis. Figure B2 shows the same weaker cat_{pres} 1 TC as in Fig. 6 but here at an early stage. In all storm snapshots, the eyewall is less clearly built up and the storm size is relatively small. Nevertheless, the algorithm manages to estimate the eyewall location and the overall storm extent. However, especially in the south-western quadrant, the distance between eyewall and storm border for both storms is relatively small, causing data extrapolation in the normalization process.

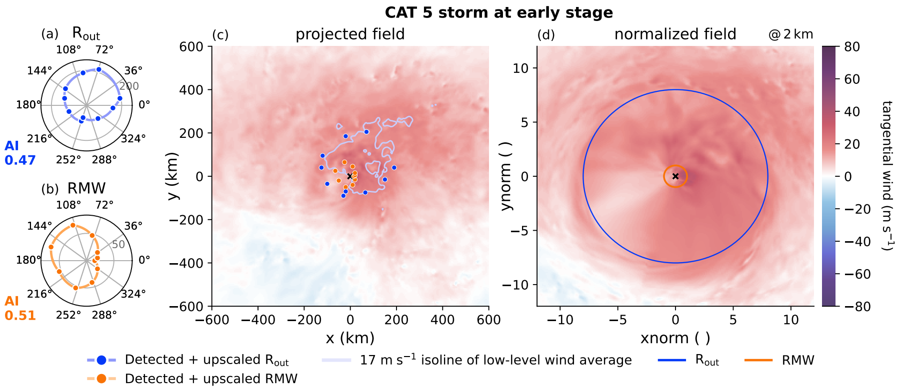

Figure B1. As Fig. 5, but short after genesis ($t_{norm} = 0.05$).

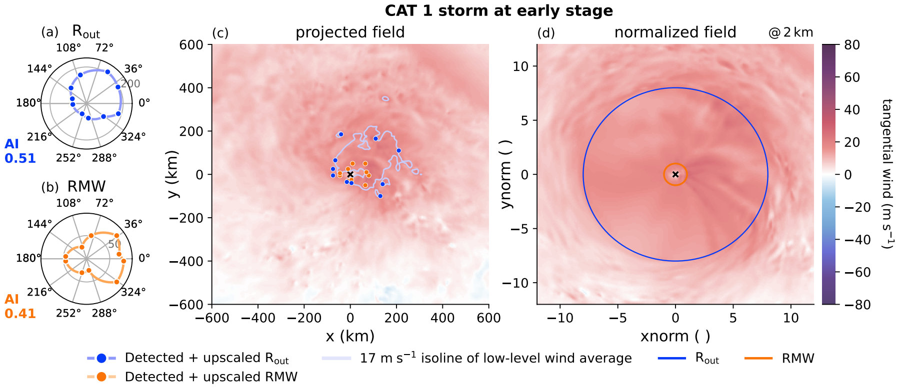

Figure B2. As Fig. 5, but for a $\mathrm{cat}_{\mathrm{pres}}$ 1 storm short after genesis ($t_{norm} = 0.05$).

Appendix C: Composite comparison

Figures C1, C2 and C3 provide a composite comparison of additional variables. Figure C1 illustrates the benefits of the SyNC composites for intense TCs. Figures C2 and C3 illustrate the benefits for weak TCs.

https://doi.org/10.5194/egusphere-2025-6186
Preprint. Discussion started: 2 February 2026

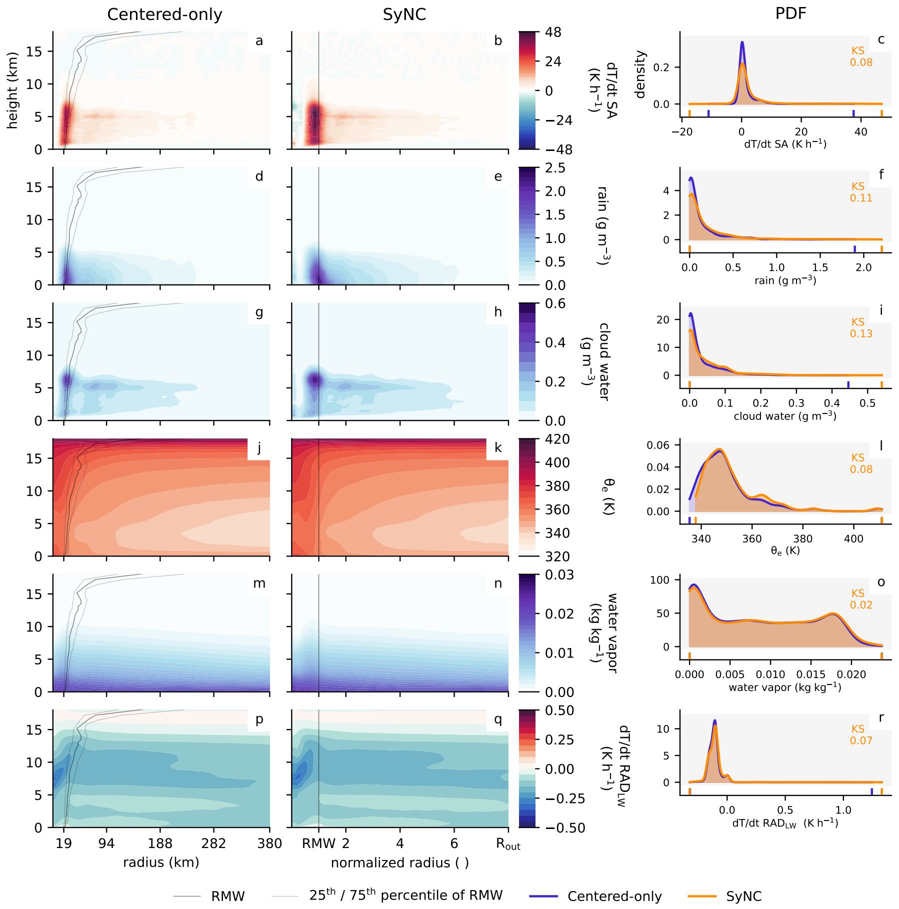

Figure C1. As Fig. 8, but for temperature tendencies due to saturation adjustment (dT/dt SA, **a**-**c**), rain mass (**d**-**f**), cloud water (**g**-**i**), equivalent potential temperature (θ_e, **j**-**l**), water vapor (**m**-**o**) and temperature tendency due to longwave radiation emission (**p**-**r**).

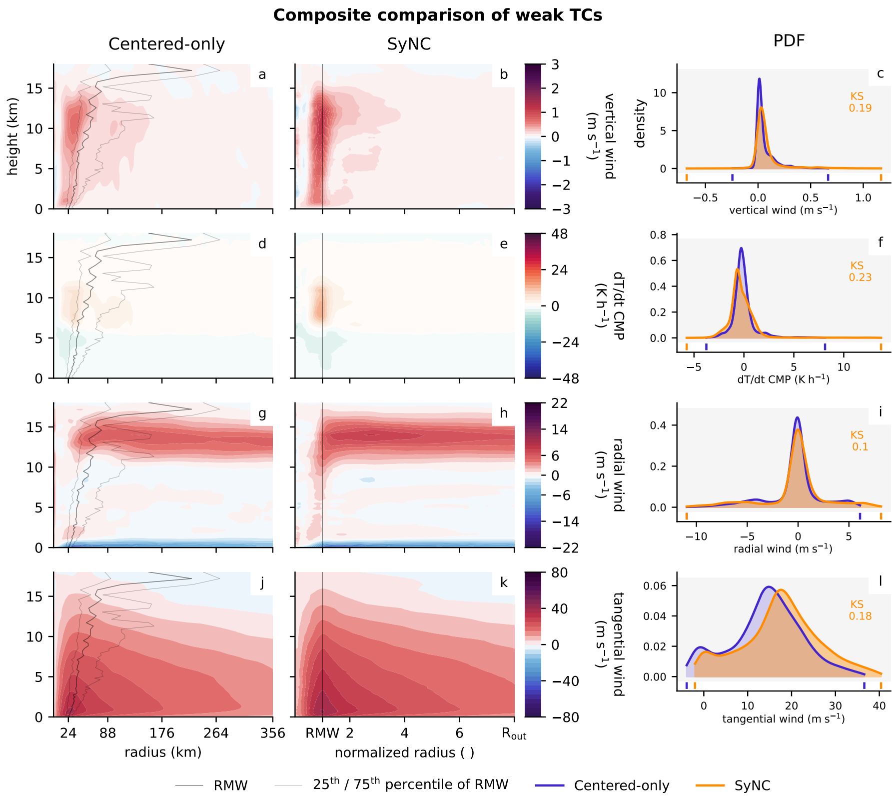

Figure C2. As Fig. 8, but for weak storms.

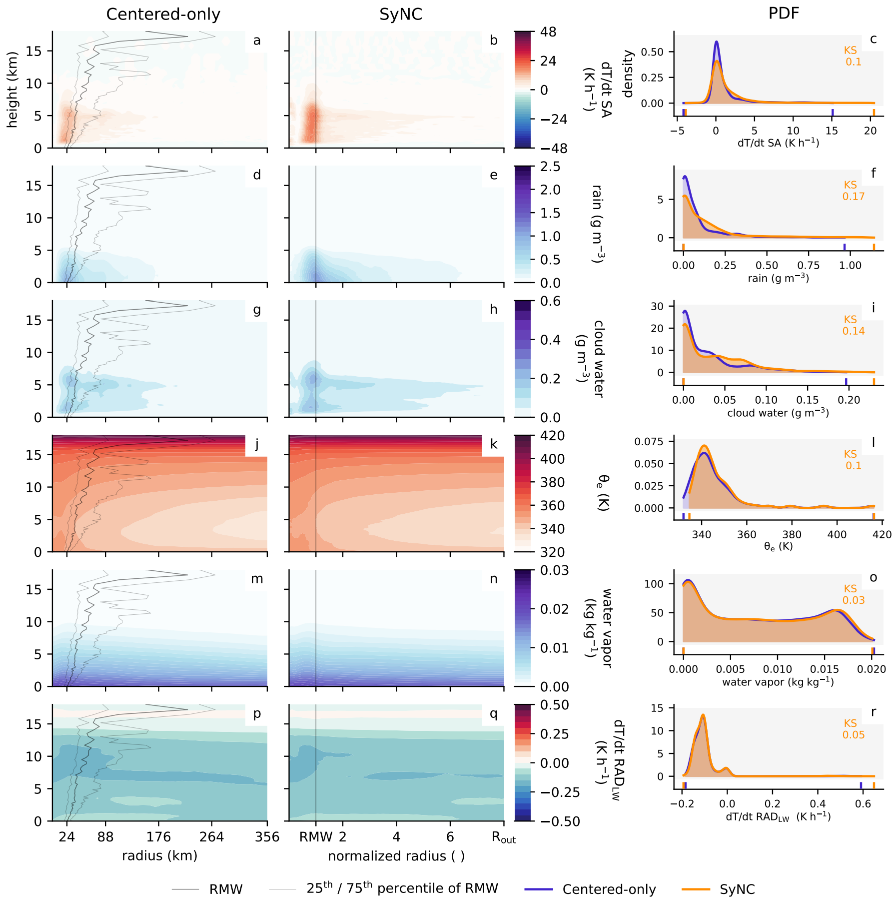

Figure C3. As Fig. 8, but for weak storms: temperature tendencies due to saturation adjustment (dT/dt SA, **a**-**c**), rain mass (**d**-**f**), cloud water (**g**-**i**), equivalent potential temperature (θ_e, **j**-**l**), water vapor (**m**-**o**) and temperature tendency due to longwave radiation emission (**p**-**r**).

Code and data availability. The model data used in this study is publicly available on Zenodo under https://doi.org/10.5281/zenodo.17865089 (Caratsch et al., 2025a). The SyNC code and scripts for data processing, analysis, and figure generation in this study is openly available on Zenodo under https://doi.org/10.5281/zenodo.17853183 (Caratsch et al., 2025b). The open-source ICON model code version 2024.10 used for our simulations can be obtained at https://icon-model.org/.

Author contributions. Model simulations, data processing and visualizations were conducted by AC. The composite method was developed by AC under the supervision of SF and UL, who provided conceptual guidance. All authors interpreted the results. The manuscript was written by AC and reviewed and edited by SF and UL.

Competing interests. The authors declare that they have no conflict of interest.

490 *Acknowledgements.* This research has been supported by the European Union's Horizon Europe program, project CleanCloud (grant agreement 101137639). The computational resources for the simulations and data processing were provided by Swiss National Supercomputing Centre (CSCS, project ID lp88). Microsoft Copilot AI was used for proofreading this manuscript.

References

Bao, J.-W., Gopalakrishnan, S. G., Michelson, S. A., Marks, F. D., and Montgomery, M. T.: Impact of Physics Representations in the HWRFX on Simulated Hurricane Structure and Pressure–Wind Relationships, Monthly Weather Review, 140, 3278–3299, https://doi.org/10.1175/MWR-D-11-00332.1, publisher: American Meteorological Society Section: Monthly Weather Review, 2012.

Bengtsson, L., Hodges, K. I., Esch, M., Keenlyside, N., Kornblueh, L., Luo, J.-J., and Yamagata, T.: How may tropical cyclones change in a warmer climate?, Tellus A: Dynamic Meteorology and Oceanography, 59, 539–561, https://doi.org/10.1111/j.1600-0870.2007.00251.x, 2007.

Bengtsson, L., Hodges, K. I., and Keenlyside, N.: Will Extratropical Storms Intensify in a Warmer Climate?, Journal of Climate, 22, 2276–2301, https://doi.org/10.1175/2008JCLI2678.1, publisher: American Meteorological Society Section: Journal of Climate, 2009.

Benjamini, Y. and Hochberg, Y.: Controlling the False Discovery Rate: A Practical and Powerful Approach to Multiple Testing, Journal of the Royal Statistical Society: Series B (Methodological), 57, 289–300, https://doi.org/10.1111/j.2517-6161.1995.tb02031.x, 1995.

Binder, H., Boettcher, M., Joos, H., and Wernli, H.: The Role of Warm Conveyor Belts for the Intensification of Extratropical Cyclones in Northern Hemisphere Winter, Journal of the Atmospheric Sciences, 73, 3997–4020, https://doi.org/10.1175/JAS-D-15-0302.1, publisher: American Meteorological Society Section: Journal of the Atmospheric Sciences, 2016.

Bourdin, S., Fromang, S., Caubel, A., Ghattas, J., Meurdesoif, Y., and Dubos, T.: Tropical cyclones in global high-resolution simulations using the IPSL model, Climate Dynamics, 62, 4343–4368, https://doi.org/10.1007/s00382-024-07138-w, 2024.

Caratsch, A., Ferrachat, S., and Lohmann, U.: Data for publication "Composite Sharpening by Vortex Symmetrization and Normalization of Tropical Cyclones", https://doi.org/10.5281/zenodo.17865089, 2025a.

Caratsch, A., Ferrachat, S., and Lohmann, U.: Scripts for publication "Composite Sharpening by Vortex Symmetrization and Normalization of Tropical Cyclones", https://doi.org/10.5281/zenodo.17853183, 2025b.

Carstens, J. D., Didlake, A. C., and Zarzycki, C. M.: Tropical Cyclone Wind Shear-Relative Asymmetry in Reanalyses, Journal of Climate, 37, 5793–5816, https://doi.org/10.1175/JCLI-D-23-0628.1, 2024.

Chan, K. T. F. and Chan, J. C. L.: Size and Strength of Tropical Cyclones as Inferred from QuikSCAT Data, Monthly Weather Review, 140, 811–824, https://doi.org/10.1175/MWR-D-10-05062.1, publisher: American Meteorological Society Section: Monthly Weather Review, 2012.

Chan, K. T. F., Zhang, K., and Xu, L.: Tropical cyclone size asymmetry index and climatology, Climate Dynamics, 61, 5049–5064, https://doi.org/10.1007/s00382-023-06840-5, 2023.

Choudhury, G. and Tesche, M.: A first global height-resolved cloud condensation nuclei data set derived from spaceborne lidar measurements, Earth System Science Data, 15, 3747–3760, https://doi.org/10.5194/essd-15-3747-2023, publisher: Copernicus GmbH, 2023.

Dacre, H. F., Hawcroft, M. K., Stringer, M. A., and Hodges, K. I.: An Extratropical Cyclone Atlas: A Tool for Illustrating Cyclone Structure and Evolution Characteristics, Bulletin of the American Meteorological Society, 93, 1497–1502, https://doi.org/10.1175/BAMS-D-11-00164.1, publisher: American Meteorological Society Section: Bulletin of the American Meteorological Society, 2012.

Dolling, K. P. and Barnes, G. M.: The Creation of a High Equivalent Potential Temperature Reservoir in Tropical Storm Humberto (2001) and Its Possible Role in Storm Deepening, Monthly Weather Review, 140, 492–505, https://doi.org/10.1175/MWR-D-11-00068.1, publisher: American Meteorological Society Section: Monthly Weather Review, 2012.

Emanuel, K. A.: The power of a hurricane: An example of reckless driving on the information superhighway, Weather, 54, 107–108, https://doi.org/10.1002/j.1477-8696.1999.tb06435.x, 1999.

Enz, B. M., Engelmann, J. P., and Lohmann, U.: Use of threshold parameter variation for tropical cyclone tracking, Geoscientific Model Development, 16, 5093–5112, https://doi.org/10.5194/gmd-16-5093-2023, publisher: Copernicus GmbH, 2023.

Fischer, E. M., Beyerle, U., Bloin-Wibe, L., Gessner, C., Humphrey, V., Lehner, F., Pendergrass, A. G., Sippel, S., Zeder, J., and Knutti, R.: Storylines for unprecedented heatwaves based on ensemble boosting, Nature Communications, 14, 4643, https://doi.org/10.1038/s41467-023-40112-4, publisher: Nature Publishing Group, 2023.

Hanley, D., Molinari, J., and Keyser, D.: A Composite Study of the Interactions between Tropical Cyclones and Upper-Tropospheric Troughs, Monthly Weather Review, 129, 2570–2584, https://doi.org/10.1175/1520-0493(2001)129<2570:ACSOTI>2.0.CO;2, 2001.

Hogan, R. J. and Bozzo, A.: A Flexible and Efficient Radiation Scheme for the ECMWF Model, Journal of Advances in Modeling Earth Systems, 10, 1990–2008, https://doi.org/10.1029/2018MS001364, 2018.

Hohenegger, C., Kornblueh, L., Klocke, D., Becker, T., Cioni, G., Engels, J. F., Schulzweida, U., and Stevens, B.: Climate Statistics in Global Simulations of the Atmosphere, from 80 to 2.5 km Grid Spacing, Journal of the Meteorological Society of Japan. Ser. II, 98, 73–91, https://doi.org/10.2151/jmsj.2020-005, 2020.

Hohenegger, C., Korn, P., Linardakis, L., Redler, R., Schnur, R., Adamidis, P., Bao, J., Bastin, S., Behravesh, M., Bergemann, M., Biercamp, J., Bockelmann, H., Brokopf, R., Brüggemann, N., Casaroli, L., Chegini, F., Datseris, G., Esch, M., George, G., Giorgetta, M., Gutjahr, O., Haak, H., Hanke, M., Ilyina, T., Jahns, T., Jungclaus, J., Kern, M., Klocke, D., Kluft, L., Kölling, T., Kornblueh, L., Kosukhin, S., Kroll, C., Lee, J., Mauritsen, T., Mehlmann, C., Mieslinger, T., Naumann, A. K., Paccini, L., Peinado, A., Praturi, D. S., Putrasahan, D., Rast, S., Riddick, T., Roeber, N., Schmidt, H., Schulzweida, U., Schütte, F., Segura, H., Shevchenko, R., Singh, V., Specht, M., Stephan, C. C., von Storch, J.-S., Vogel, R., Wengel, C., Winkler, M., Ziemen, F., Marotzke, J., and Stevens, B.: ICON-Sapphire: simulating the components of the Earth system and their interactions at kilometer and subkilometer scales, Geoscientific Model Development, 16, 779–811, https://doi.org/10.5194/gmd-16-779-2023, publisher: Copernicus GmbH, 2023.

Holland, G. J.: The Maximum Potential Intensity of Tropical Cyclones, Journal of the Atmospheric Sciences, 54, 2519–2541, https://doi.org/10.1175/1520-0469(1997)054<2519:TMPIOT>2.0.CO;2, publisher: American Meteorological Society Section: Journal of the Atmospheric Sciences, 1997.

Judt, F., Klocke, D., Rios-Berrios, R., Vanniere, B., Ziemen, F., Auger, L., Biercamp, J., Bretherton, C., Chen, X., Düben, P., Hohenegger, C., Khairoutdinov, M., Kodama, C., Kornblueh, L., Lin, S.-J., Nakano, M., Neumann, P., Putman, W., Röber, N., Roberts, M., Satoh, M., Shibuya, R., Stevens, B., Vidale, P. L., Wedi, N., and Zhou, L.: Tropical Cyclones in Global Storm-Resolving Models, Journal of the Meteorological Society of Japan. Ser. II, 99, 579–602, https://doi.org/10.2151/jmsj.2021-029, 2021.

Juračić, A. and Raymond, D. J.: The effects of moist entropy and moisture budgets on tropical cyclone development, Journal of Geophysical Research: Atmospheres, 121, 9458–9473, https://doi.org/10.1002/2016JD025065, 2016.

Kepert, J. D.: Tropical Cyclone Structure and Dynamics, in: Global Perspectives on Tropical Cyclones, vol. Volume 4 of *World Scientific Series on Asia-Pacific Weather and Climate*, pp. 3–53, WORLD SCIENTIFIC, ISBN 978-981-4293-47-1, https://doi.org/10.1142/9789814293488_0001, 2010.

Kepert, J. D. and Chan, J. C. L.: Global perspectives on tropical cyclones: from science to mitigation, World scientific series on Asia-Pacific weather and climate, World scientific, London, ISBN 978-981-4293-47-1, https://doi.org/10.1142/7597, 2010.

Klotz, B. W. and Jiang, H.: Examination of Surface Wind Asymmetries in Tropical Cyclones. Part I: General Structure and Wind Shear Impacts, Monthly Weather Review, 145, 3989–4009, https://doi.org/10.1175/MWR-D-17-0019.1, 2017.

Klotzbach, P. J., Bell, M. M., Bowen, S. G., Gibney, E. J., Knapp, K. R., and Schreck, C. J.: Surface Pressure a More Skillful Predictor of Normalized Hurricane Damage than Maximum Sustained Wind, Bulletin of the American Meteorological Society, 101, E830–E846, https://doi.org/10.1175/BAMS-D-19-0062.1, publisher: American Meteorological Society Section: Bulletin of the American Meteorological Society, 2020.

Knutson, T. R., Sirutis, J. J., Zhao, M., Tuleya, R. E., Bender, M., Vecchi, G. A., Villarini, G., and Chavas, D.: Global Projections of Intense Tropical Cyclone Activity for the Late Twenty-First Century from Dynamical Downscaling of CMIP5/RCP4.5 Scenarios, Journal of Climate, 28, 7203–7224, https://doi.org/10.1175/JCLI-D-15-0129.1, publisher: American Meteorological Society Section: Journal of Climate, 2015.

Krzywinski, M. and Altman, N.: Analysis of variance and blocking, Nature Methods, 11, 699–700, https://doi.org/10.1038/nmeth.3005, 2014.

Landsea, C. W. and Franklin, J. L.: Atlantic Hurricane Database Uncertainty and Presentation of a New Database Format, Monthly Weather Review, 141, 3576–3592, https://doi.org/10.1175/MWR-D-12-00254.1, publisher: American Meteorological Society Section: Monthly Weather Review, 2013.

Li, H. and Tang, X.: Outer-core size asymmetry and intensification of North Atlantic tropical cyclones, Atmospheric Research, 322, 108 131, https://doi.org/10.1016/j.atmosres.2025.108131, 2025.

Lin, Y., Wang, Y., Hsieh, J.-S., Jiang, J. H., Su, Q., Zhao, L., Lavallee, M., and Zhang, R.: Assessing the destructiveness of tropical cyclones induced by anthropogenic aerosols in an atmosphere–ocean coupled framework, Atmospheric Chemistry and Physics, 23, 13 835–13 852, https://doi.org/10.5194/acp-23-13835-2023, publisher: Copernicus GmbH, 2023.

Martinez, J., Davis, C. A., and Bell, M. M.: Eyewall Asymmetries and Their Contributions to the Intensification of an Idealized Tropical Cyclone Translating in Uniform Flow, Journal of the Atmospheric Sciences, 79, 2471–2491, https://doi.org/10.1175/JAS-D-21-0302.1, 2022.

Ming, J., Zhang, J., and Rogers, R.: Typhoon kinematic and thermodynamic boundary layer structure from dropsonde composites: TYPHOON BL STRUCTURE FROM DROPSONDE, Journal of Geophysical Research: Atmospheres, 120, https://doi.org/10.1002/2014JD022640, 2015.

Ohno, T. and Satoh, M.: On the Warm Core of a Tropical Cyclone Formed near the Tropopause, Journal of the Atmospheric Sciences, 72, 551–571, https://doi.org/10.1175/JAS-D-14-0078.1, publisher: American Meteorological Society Section: Journal of the Atmospheric Sciences, 2015.

Persing, J., Montgomery, M. T., McWilliams, J. C., and Smith, R. K.: Asymmetric and axisymmetric dynamics of tropical cyclones, Atmospheric Chemistry and Physics, 13, 12 299–12 341, https://doi.org/10.5194/acp-13-12299-2013, 2013.

Qin, N., Zhang, D.-L., and Li, Y.: A Statistical Analysis of Steady Eyewall Sizes Associated with Rapidly Intensifying Hurricanes, Weather and Forecasting, 31, 737–742, https://doi.org/10.1175/WAF-D-16-0016.1, publisher: American Meteorological Society Section: Weather and Forecasting, 2016.

Raschendorfer, M.: The new turbulence parameterization of LM, COSMO Newsletter, No. 1, http://www.cosmo-model.org/content/model/documentation/newsLetters/newsLetter01/newsLetter_01.pdf, 2001.

Reed, K. A., Bacmeister, J. T., Rosenbloom, N. A., Wehner, M. F., Bates, S. C., Lauritzen, P. H., Truesdale, J. E., and Hannay, C.: Impact of the dynamical core on the direct simulation of tropical cyclones in a high-resolution global model, Geophysical Research Letters, 42, 3603–3608, https://doi.org/10.1002/2015GL063974, 2015.

Rios-Berrios, R. and Torn, R. D.: Climatological Analysis of Tropical Cyclone Intensity Changes under Moderate Vertical Wind Shear, Monthly Weather Review, 145, 1717–1738, https://doi.org/10.1175/MWR-D-16-0350.1, publisher: American Meteorological Society Section: Monthly Weather Review, 2017.

Rosenfeld, D., Woodley, W. L., Khain, A., Cotton, W. R., Carrió, G., Ginis, I., and Golden, J. H.: Aerosol Effects on Microstructure and Intensity of Tropical Cyclones, Bulletin of the American Meteorological Society, 93, 987–1001, https://doi.org/10.1175/BAMS-D-11-00147.1, publisher: American Meteorological Society Section: Bulletin of the American Meteorological Society, 2012.

Schemm, S., Sprenger, M., and Wernli, H.: When during Their Life Cycle Are Extratropical Cyclones Attended by Fronts?, Bulletin of the American Meteorological Society, 99, 149–165, https://doi.org/10.1175/BAMS-D-16-0261.1, publisher: American Meteorological Society Section: Bulletin of the American Meteorological Society, 2018.

Schulz, J.-P., Vogel, G., Becker, C., Kothe, S., Rummel, U., and Ahrens, B.: Evaluation of the ground heat flux simulated by a multi-layer land surface scheme using high-quality observations at grass land and bare soil, Meteorologische Zeitschrift, pp. 607–620, https://doi.org/10.1127/metz/2016/0537, publisher: Schweizerbart'sche Verlagsbuchhandlung, 2016.

Segal, Y. and Khain, A.: Dependence of droplet concentration on aerosol conditions in different cloud types: Application to droplet concentration parameterization of aerosol conditions, Journal of Geophysical Research: Atmospheres, 111, https://doi.org/10.1029/2005JD006561, 2006.

Segura, H., Pedruzo-Bagazgoitia, X., Weiss, P., Müller, S. K., Rackow, T., Lee, J., Dolores-Tesillos, E., Benedict, I., Aengenheyster, M., Aguridan, R., Arduini, G., Baker, A. J., Bao, J., Bastin, S., Baulenas, E., Becker, T., Beyer, S., Bockelmann, H., Brüggemann, N., Brunner, L., Cheedela, S. K., Das, S., Denissen, J., Dragaud, I., Dziekan, P., Ekblom, M., Engels, J. F., Esch, M., Forbes, R., Frauen, C., Freischem, L., García-Maroto, D., Geier, P., Gierz, P., González-Cervera, , Grayson, K., Griffith, M., Gutjahr, O., Haak, H., Hadade, I., Haslehner, K., Ul Hasson, S., Hegewald, J., Kluft, L., Koldunov, A., Koldunov, N., Kölling, T., Koseki, S., Kosukhin, S., Kousal, J., Kuma, P., Kumar, A. U., Li, R., Maury, N., Meindl, M., Milinski, S., Mogensen, K., Niraula, B., Nowak, J., Praturi, D. S., Proske, U., Putrasahan, D., Redler, R., Santuy, D., Sármány, D., Schnur, R., Scholz, P., Sidorenko, D., Spät, D., Sützl, B., Takasuka, D., Tompkins, A., Uribe, A., Valentini, M., Veerman, M., Voigt, A., Warnau, S., Wachsmann, F., Wacławczyk, M., Wedi, N., Wieners, K.-H., Wille, J., Winkler, M., Wu, Y., Ziemen, F., Zimmermann, J., Bender, F. A.-M., Bojovic, D., Bony, S., Bordoni, S., Brehmer, P., Dengler, M., Dutra, E., Faye, S., Fischer, E., Van Heerwaarden, C., Hohenegger, C., Järvinen, H., Jochum, M., Jung, T., Jungclaus, J. H., Keenlyside, N. S., Klocke, D., Konow, H., Klose, M., Malinowski, S., Martius, O., Mauritsen, T., Mellado, J. P., Mieslinger, T., Mohino, E., Pawłowska, H., Peters-von Gehlen, K., Sarré, A., Sobhani, P., Stier, P., Tuppi, L., Vidale, P. L., Sandu, I., and Stevens, B.: nextGEMS: entering the era of kilometer-scale Earth system modeling, https://doi.org/10.5194/egusphere-2025-509, 2025.

Seifert, A. and Beheng, K. D.: A two-moment cloud microphysics parameterization for mixed-phase clouds. Part 1: Model description, Meteorology and Atmospheric Physics, 92, 45–66, https://doi.org/10.1007/s00703-005-0112-4, 2006.

Sinclair, V., Rantanen, M., Haapanala, P., Räisänen, J., and Järvinen, H.: The characteristics and structure of extra-tropical cyclones in a warmer climate, Weather and Climate Dynamics, 1, 1–25, https://doi.org/10.5194/wcd-1-1-2020, 2020.

Smith, R. K.: Tropical Cyclones: Observations and Basic Processes, 2024.

Stern, D. P., Vigh, J. L., Nolan, D. S., and Zhang, F.: Revisiting the Relationship between Eyewall Contraction and Intensification, Journal of the Atmospheric Sciences, 72, 1283–1306, https://doi.org/10.1175/JAS-D-14-0261.1, publisher: American Meteorological Society Section: Journal of the Atmospheric Sciences, 2015.

Sun, Z., Zhang, B., Zhang, J. A., and Perrie, W.: Examination of Surface Wind Asymmetry in Tropical Cyclones over the Northwest Pacific Ocean Using SMAP Observations, Remote Sensing, 11, 2604, https://doi.org/10.3390/rs11222604, number: 22 Publisher: Multidisciplinary Digital Publishing Institute, 2019.

https://doi.org/10.5194/egusphere-2025-6186
Preprint. Discussion started: 2 February 2026

Trier, S. B., Ahijevych, D. A., Carroll-Smith, D., Bryan, G. H., and Edwards, R.: Composite Mesoscale Environmental Conditions Influencing Tornado Frequencies in Landfalling Tropical Cyclones, Weather and Forecasting, 38, 2481–2508, https://doi.org/10.1175/WAF-D-22-0227.1, publisher: American Meteorological Society Section: Weather and Forecasting, 2023.

Uhlhorn, E. W., Klotz, B. W., Vukicevic, T., Reasor, P. D., and Rogers, R. F.: Observed Hurricane Wind Speed Asymmetries and Relationships to Motion and Environmental Shear, Monthly Weather Review, 142, 1290–1311, https://doi.org/10.1175/MWR-D-13-00249.1, publisher: American Meteorological Society Section: Monthly Weather Review, 2014.

Ventura, V., Paciorek, C. J., and Risbey, J. S.: Controlling the Proportion of Falsely Rejected Hypotheses when Conducting Multiple Tests with Climatological Data, Journal of Climate, 17, 4343–4356, https://doi.org/10.1175/3199.1, publisher: American Meteorological Society Section: Journal of Climate, 2004.

Vessey, A. F., Hodges, K. I., Shaffrey, L. C., and Day, J. J.: The composite development and structure of intense synoptic-scale Arctic cyclones, Weather and Climate Dynamics, 3, 1097–1112, https://doi.org/10.5194/wcd-3-1097-2022, publisher: Copernicus GmbH, 2022.

Wang, Y., Lee, K.-H., Lin, Y., Levy, M., and Zhang, R.: Distinct effects of anthropogenic aerosols on tropical cyclones, Nature Climate Change, 4, 368–373, https://doi.org/10.1038/nclimate2144, 2014.

Wei, C., Zhao, X., Liu, Y., Yang, P., Zhou, Z., and Chen, Y.: Bias Analysis and Correction of ERA5 Reanalysis in the Context of Tropical Cyclones, Journal of Geophysical Research: Atmospheres, 130, e2024JD042 737, https://doi.org/10.1029/2024JD042737, 2025.

Weiss, P., Herbert, R., and Stier, P.: ICON-HAM-lite 1.0: simulating the Earth system with interactive aerosols at kilometer scales, Geoscientific Model Development, 18, 3877–3894, https://doi.org/10.5194/gmd-18-3877-2025, publisher: Copernicus GmbH, 2025.

Wilks, D. S.: Statistical Methods in the Atmospheric Sciences, Academic Press, ISBN 978-0-12-385023-2, google-Books-ID: fx-PiH9Ef9VoC, 2011.

Yu, C.-K., Lin, C.-Y., and Pun, C.-H.: Origin of outer tropical cyclone rainbands, Nature Communications, 14, 7061, https://doi.org/10.1038/s41467-023-42896-x, 2023.

Zhang, F. and Tao, D.: Effects of Vertical Wind Shear on the Predictability of Tropical Cyclones, Journal of the Atmospheric Sciences, 70, 975–983, https://doi.org/10.1175/JAS-D-12-0133.1, 2013.

Zhang, J. A., Rogers, R. F., Reasor, P. D., Uhlhorn, E. W., and Marks, F. D.: Asymmetric Hurricane Boundary Layer Structure from Dropsonde Composites in Relation to the Environmental Vertical Wind Shear, Monthly Weather Review, 141, 3968–3984, https://doi.org/10.1175/MWR-D-12-00335.1, 2013.

Zängl, G., Reinert, D., Rípodas, P., and Baldauf, M.: The ICON (ICOsahedral Non-hydrostatic) modelling framework of DWD and MPI-M: Description of the non-hydrostatic dynamical core, Quarterly Journal of the Royal Meteorological Society, 141, 563–579, https://doi.org/10.1002/qj.2378, 2015.